Quantum experiments with single-photon spin-orbit lattice arrays

by

Ruoxuan Xu

A thesis
presented to the University of Waterloo
in fulfillment of the
thesis requirement for the degree of
Master of Applied Science
in
Electrical and Computer Engineering

Waterloo, Ontario, Canada, 2019

Author's Declaration

I hereby declare that I am the sole author of this thesis. This is a true copy of the thesis, including any required final revisions, as accepted by my examiners.

I understand that my thesis may be made electronically available to the public.

Abstract

The thesis introduces two single-photon experiments with the lattice of spin-orbit arrays. The basic background knowledge has been introduced in Chapter 1. Chapters $2-4$ describe the detailed techniques used in these two experiments.

In the first work, we implement a remote state preparation protocol on our single-photon orbital angular momentum (OAM) lattice state via hybrid-entanglement. Remote state preparation is a variant of quantum state teleportation where the sender knows the transmitted state. It is known to require fewer classical resources and exhibit a nontrivial trade-off between the entanglement and classical communication compared with quantum teleportation. Here we propose a state preparation scheme between two spatially separated photons sharing a hybrid-entangled polarization-OAM state. By sending one of the polarization-entangled photon pairs through Lattice of Optical Vortex prism pairs, we generate a two-dimensional lattice of spin-orbit coupled single-photons. We show that the measurement taken by an electron-multiplying intensified CCD camera on the transformed photons can be remotely prepared by the polarization projection of the other. Our protocol could have a significant impact on long-distance quantum communication with higher channel capacity and lead to more efficient and compatible quantum information processing techniques.

The second experiment investigates the single-photon Talbot Effect in spin-orbit arrays. The Talbot Effect is a near-field diffraction effect, that occurs with the propagation of periodically structured waves. It has enabled several unique applications in optical metrology, image processing, data transmission, and matter-wave interferometry. We observe that upon propagation, the wavefronts of the single photons manifest self-imaging whereby the OAM lattice intensity profile is recovered. Furthermore, we show that the intensity distribution at each fractional Talbot distance is indicative of the periodic helical phase structure corresponding to a lattice of OAM states. This phenomenon is a significant addition to the toolbox of orbital angular momentum and spin-orbit techniques that are becoming increasingly important in optical implementations of quantum information.

Acknowledgements

I would like to express my gratitude to so many lovely people I met in Waterloo these two years. Without them, none of these is possible. Many thanks to my supervisor Kevin Resch who has been giving me support and attention throughout my master's study. Thanks for giving me lots of freedom when studying courses, working on the project and learning new skills. I am grateful for your scientific vision and starting me out in the quantum world. Thank you to my committee members, Michal Bajcsy, Guoxing Miao and Chris Wilson for helping me finish my Master's work.

Thanks to my sweet lab mates and colleagues in IQC. Special thanks to Jean-Philippe Maclean and Andrew Cameron for helping me get started in this wonderful lab. Thanks so much for Sacha Schwarz for giving me a lot of guidance and being my everyday consultant throughout my project and also share me funny stories about Switzerland. Thanks to all other lab mates, Patrick Daley, Morgan Mastrovich, Matt Brown and Mike Mazurek. There are also other IQC members that I have a chance to work with, Katanya Kuntz, Connor Kapahi, Dmitry Pushin and Dusan Sarenac. Special thanks also go to so many friends I made in IQC who bring me laughter in the busy graduate life. Still remember the time Youn Seok Lee taught me daily Korean sentences and shared traditional Korean food with me.

Also, thanks to all my ECE classmates met in class and I enjoy the time we studying, doing assignments, working on interesting projects and of course preparing for final exams together. Thanks to all my roommates and friends who make me feel the warmth of home, Masijia Qiu, Shuting Lian, Yu huang, Peyton Shi, Hsuan-Han Huang, Ruifan Yu, Gilbert Shih, Martinet Lee, etc.

Last but least, thanks to my parents for all the constant support and encouragement you have given me. Keep moving on for the rest of life.

Dedication

This is dedicated to my parents for endless love, trust and encouragement.

Table of Contents

List of Figures

Chapter 1

Introduction

1.1 Quantum bit—representation and operation

The quantum bit or qubit is the basic unit of quantum information, analogous to the bit for classcial information. It can be realized using any quantum physical system with two orthogonal states. For example, horizontal and vertical polarization of a photon, spin-up and spin-down of an electron or two energy levels of an atom. It can be described as a two component vector regardless of the physical implementation.

1.1.1 Mathematical representation

A bit is in either the state 0 or 1. A qubit state can be in the $|0\rangle$ or $|1\rangle$, but can also be in a superposition state which can be represented mathematically as a linear combination of two states:

$$|\psi\rangle = \alpha|0\rangle + \beta|1\rangle, \tag{1.1}$$

where α and β are complex coefficients. These coefficients here are referred to as amplitudes and computational basis $|0\rangle$ and $|1\rangle$ are called "ket" and refer to the two computational basis states. The probability for measuring the outcomes 0 and 1 are given by $|\alpha|^2$ and $|\beta|^2$ where

$$|\alpha|^2 + |\beta|^2 = 1. \tag{1.2}$$

Qubits are often represented on the Bloch Sphere. The coefficients here are normalized to one meaning it is a pure state that can be represented on the surface of the Bloch Sphere

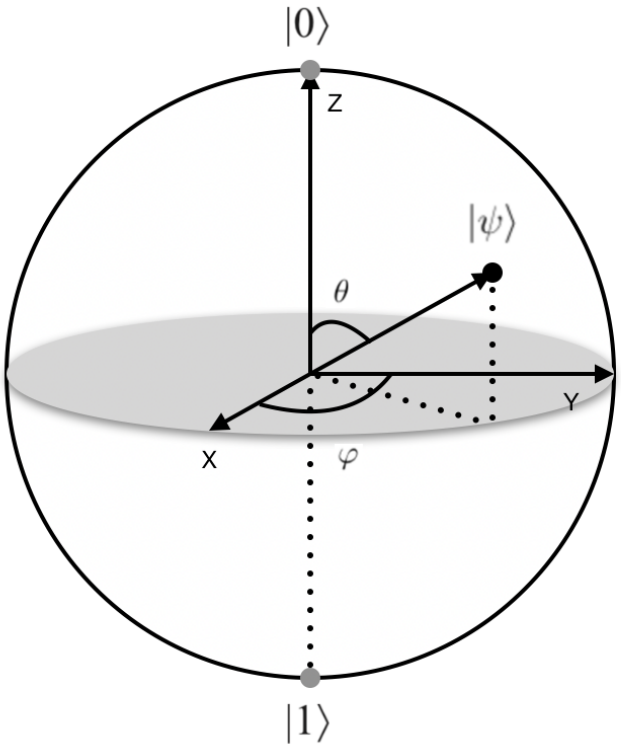

Figure 1.1: Single qubit represented in Bloch sphere

as shown in Fig. 1.1. This three-dimensional geometric representation helps visualize the useful information for the state of a single qubit [89, 69].

We can also rewrite Eq. (1.1) to explicitly enforce normalization:

$$|\psi\rangle = e^{i\gamma}\left(\cos\frac{\theta}{2}|0\rangle + e^{i\psi}\sin\frac{\theta}{2}|1\rangle\right) \tag{1.3}$$

where θ, ψ and γ are real numbers. Since the factor $e^{i\gamma}$ has no observable effects, it can be dropped and only two real parameters θ and ψ are left constituting the direction of the vectors (states) in unit three dimensional sphere shown in Fig. 1.1.

We can generalize to n-qubits systems with the form

$$|\psi\rangle = \sum_{i=00\ldots0}^{11\ldots1} c_x|x\rangle \tag{1.4}$$

where c_x are complex number and $\sum |c_x|^2 = 1$. Therefore, the quantum state of an n-qubits system is specified by 2^n amplitudes in an exponentially growing Hilbert space.

The measurement outcomes depend distinctly on different properties of the qubit state to experimental verify and manipulate them.

1.1.2 Operation on qubits

Any quantum operations can be expressed as a sequence of one-qubit and two-qubit quantum gates [8].

For one-qubits, they may perform any single-qubit unitary operators through rotations of the Bloch sphere. Many properties of operators can be expressed in terms of their representative matrices. For example, the Identity operator which is often denoted as I keeps the state unchanged. Its matrix representation, irrespective of the choice of basis states, has the format where the diagonal elements are all unity and the off-diagonal elements are all zero. Rotations around the x,y,z axis can be generated through Pauli matrices σ_x, σ_y, σ_y. These are 2 by 2 matrices that are very useful in quantum information field. Their matrices and corresponding notations are shown in Eq. (1.5):

$$\sigma_x = \begin{bmatrix} 0 & 1 \\ 1 & 0 \end{bmatrix} \quad \sigma_y = \begin{bmatrix} 0 & -i \\ i & 0 \end{bmatrix} \quad \sigma_z = \begin{bmatrix} 1 & 0 \\ 0 & -1 \end{bmatrix}. \tag{1.5}$$

Apart from Pauli matrices, the Hadamard gate is also a useful quantum gate. It is equal to a rotation of the sphere about y axis by 90 degrees followed by a rotation about x axis by 180 degrees. It maps the basis states $|0\rangle$ and $|1\rangle$ to $(|0\rangle + |1\rangle)/\sqrt{2}$ and $(|0\rangle - |1\rangle)/\sqrt{2}$ where the measurements on both basis state $|0\rangle$ and $|1\rangle$ have equal probability.

There are also two-qubit gates such as Swap gate and Controlled-NOT gate. Particularly, C-NOT gate perfom the NOT operation on the second qubit only when the first qubit is $|1\rangle$, otherwise leaves it unchanged. This operator can realize all unitary transformation combined with one-qubit gates.

1.2 Quantum information processing

Quantum information processing is the study of the information processing protocols accomplished using quantum mechanics systems. Quantum information has been known to

have the possibility to perform certain tasks believed to be too difficult or even impossible using classical ones. In communication, quantum information enables the secrete information transmission protected by physically guaranteed eavesdropper detection. In computation, it enables efficient simulations of quantum mechanical systems, exponential speedup for unstructured search.

As we push conventional fabrication of computer further and further into the microscopic world, quantum effects begin to appear. This led to different information processing methods no longer relying on classical physics. Many techniques on controlling single quantum systems have been developed since the goal of complete control of a single quantum system was proposed in the 1970s [29, 55, 100]. We are currently developing tools for better manipulation of single quantum systems and extending it to more complex systems.

Significant advances have made in different fields during the past few decades such as quantum simulation [73], quantum algorithm [113, 47] and quantum communication [13, 34, 83]. Small-scale quantum computers that allow dozens of operations done in a few quantum bits have already been demonstrated. Realistic long-distance quantum communication and quantum cryptography have been experimentally achieved and employed in real world.

We are still in the early days of quantum information. It provides us a better understanding of quantum mechanics and tools to sharpen our intuition about its underlying theory. It also enables the development of new applications of quantum information and builds controllable quantum devices that benefit us.

1.3 Entanglement

1.3.1 Fundamental concept and application

The phenomenon that the existence of global states of a composite system which can not be expressed as a product of the individual subsystems is known as entanglement [53]. Entanglement is of the center of quantum information protocols. This property makes quantum information processing promising and powerful but also brings many challenges. Quantum entanglement enables joint measurement of separate systems to show a stronger correlation than classically allowable. These strong than classical correlations are quantified by violations of Bell's inequality. Since the first experimental demonstration of entanglement in 1972 with photons [42], entanglement in different optical degrees of freedom (DOFs) have been studied [68, 67, 54, 78] and have been experimentally verified in many different physical systems.

Considering a two-qubits entangled state:

$$|\psi^+\rangle_{AB} = \frac{1}{\sqrt{2}} \left(|0\rangle_A |1\rangle_B - |1\rangle_A |0\rangle_B \right), \tag{1.6}$$

we describe two spatially separated parties Alice and Bob, they hold qubit A and B respectively. When either of the parties does a measurement on the qubit, they will find the two possible results occur with an equal possibility of 1/2. However, if they measure the same observers simultaneously, they get anti-correlated outcomes.

Quantum entanglement is a precious resource for quantum communication enabling new methods for quantum information transmission. The utilization of non-locality of shared entangled states can prepare a state on the remote receiver's quantum system without sending the original state physically. It can also provide exponential enhancements for pure state quantum computing [59].

1.3.2 Generation of entangled photon state

Entangled photon pairs can be generated using cascade decays in atomic systems [5] or via parametric processes involving resonant fluorescence where two pump photons create an entangled state between photon pairs. The most popular method for generating entangled photons is via spontaneous parameter down-conversion in crystals via nonlinear optics [24].

In the spontaneous down-conversion (SPDC) process, photons from a pump beam decay into pairs of photons designated as signal and idler in a nonlinear crystal. The strongly correlated two-photon pairs are under the restriction of conservation of energy (frequency):

$$\omega_1 + \omega_2 = \omega_p, \quad or \quad \vec{k}_1 + \vec{k}_2 = \vec{k}_p \tag{1.7}$$

The two down-converted photons generated using SPDC can either be energy degenerate where both 'daughter' photons are of the same energy(frequency) or it be non-degenerate. SPDC is a process for generating the signal and idler photons from the higher-frequency pump by quantum vacuum fields with a phase relationship between input and output fields.

There are two main ways which can be referred to as type I and type II phase matching to do the SPDC process. We are using the type II SPDC process for generating the signal and idler photons having perpendicular polarizations.

1.4 Encoding quantum information into photons

Photons are the optimal information carriers due to the lack of interaction with external environment and reliable techniques for generation and manipulation.

Photon-based quantum information can be encoded in the degrees of freedom of light. These can be spin-angular momentum (polarization) orbital angular momentum (spatial distribution), propagation (path encoding) [81], time-bin and time-frequency [11] *etc.* Here we focus on spin and orbital angular momentum degrees of freedom.

1.4.1 Encoding in polarization

Spin is associated with polarization degrees of freedom. Polarization encoding offers straightforward methods for preparing, manipulating and measuring quantum information. The spin-orbit momentum component of photons can interact with anisotropic transparent systems like birefringent crystals which are widely employed for polarization control [41].

The polarization state of photon is usually represented in horizontal $|H\rangle$ and vertical bases $|V\rangle$ written as $|\psi\rangle = \alpha|H\rangle + \beta|V\rangle$. Diagonal ($|D\rangle$), anti-diagonal ($|A\rangle$), left circular ($|L\rangle$) and right circular ($|R\rangle$) are other common bases where these states are defined:

$$|D/A\rangle = \frac{1}{\sqrt{2}}\left(|H\rangle \pm |V\rangle\right) \quad |L/R\rangle = \frac{1}{\sqrt{2}}\left(|H\rangle \pm i|V\rangle\right) \tag{1.8}$$

where D, A, L, R stands for diagonal, anti-diagonal, left circular, and right circular, respectively.

Polarization has played a central role in quantum information, ranging from quantum simulation [106, 82] to quantum computation [33, 101, 10, 28] and quantum communication [76, 19, 119]. However, the polarization of one photon is limited to a two-level system. One solution for this is to couple the polarization to other degrees of freedom such as orbital angular momentum which is what we do in Chapter three to give the potential for a higher-dimensional Hilbert space.

1.4.2 Encoding in orbital angular momentum

Orbital angular momentum

Orbital angular momentum (OAM) of light arises from the spatially varying amplitude and phase distribution [2, 1]. It can be divided into internal and external components. The

internal of OAM is related to twisted wavefronts which are independent of the origin. The external one is origin-dependent given $L_e = r \times P$ where P is the momentum of a beam of light.

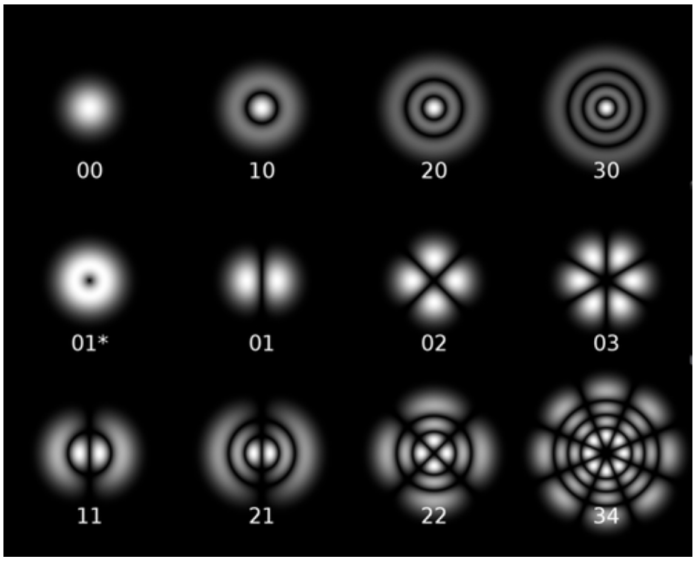

Figure 1.2: Intensity distribution of Laguerre-Gaussian modes

Light beams with an azimuthal phase carry an OAM that is independent of its spin [2]. The OAM carried by such optical vortices is described using phase factor $e^{il\phi}$ where the angle ϕ here is the angular coordinate in the plane that is transverse to the propagation direction. l here can take any positive or negative integers. Correspondingly, each single photon can carry a quantized value of $L = l\bar{h}$.

Currently, the most common form of beams with helical phase fronts is the so-called Laguerre-Gaussian mode (LG mode). LG modes are circularly symmetric and exhibit a cylindrical symmetry described by the Laguerre polynomials. The figure Fig. 1.2 shows intensity distribution of such mode. The cylindrical LG modes have an explicit phase factor which makes them a natural candidate for describing beams carrying OAM.

There are several techniques for generating and controlling the OAM. The widely employed tools are using meta-materials, cylindrical lens pairs [132], diffraction gratings [48] or Spatial Light modular (SLM) [25, 26]. SLMs can manipulate the intensity and the phase profile of the beam point by point which may have applications such as holography based optical tweezer [92, 32].

The use of OAM in quantum information enables encoding large amounts of information on a single photon. It breaks the limitation of quantum information encoding based on two-dimensional spin angular momentum associated with polarization of photons. Using OAM of photons, we can create multi-dimensional entanglement using spatial mode carrying OAM which has great potential for a higher (theoretically can be infinite) discrete quantum space encoded in a single photon [85, 91, 118, 39]. It is a method, in addition to multi-particle entanglement [125, 136], to extend the usual two-dimensional spin angular momentum quantum systems to a larger Hilbert space.

Talbot Effect with orbital angular momentum arrays

OAM can also be prepared in arrays. Generation of periodic OAM arrays coupled with spin angular momentum have been realized using linear optical components [107], nematic liquid crystal [7]. Potential application would be the use of a lattice beam structure to increase the bandwidth of data transfer using OAM modes [71, 139]. Furthermore, matching the lattice constant (period) to the characteristic length scale of the target materials could extend the OAM number selection rules across the region which is proportional to the area of the fully structured wave front [4, 51].

The periodic structure of the OAM lattice enables the Talbot Effect. The Talbot Effect is a near-field diffraction phenomenon whereby periodic phase and amplitude modulations are self-imaged due to free-space propagation. Replicas of periodic transverse intensity profile reappear after a specific propagation distance known as Talbot distance. The Talbot Effect was first observed by Henry Fox Talbot in 1836 [116]. He showed that the periodic structure repeats its pattern along the propagation direction at $z = nz_T$ where n is an integer and z_T is the Talbot distance by which the self-images reappear:

$$z_T = \frac{2a^2}{\lambda}. \tag{1.9}$$

The parameter a is the lattice constant of the periodic structured beam and λ is the wavelength. As shown in Eq. (1.9), Talbot distance is proportional to a^2 and is inversely proportional to the wavelength. Due to these characteristics, the Talbot Effect can be used in spectral reconstruction. Previous work on spectrometers utilize Talbot Effect by measuring the field intensity as a function of propagation distance have been reported [127, 102].

Fresnel diffraction of a transmission grating results in the replicas of periodic transverse intensity profile reappear after certain propagation interval [129]. These periodic pattern

of self-images are observable right behind the grating. Talbot Effect has been demonstrated in various research fields involving single photon [115, 30], x-rays [99], matter-waves [27, 31, 135, 98], exciton polaritons [43] and Bose-Einstein condensates [79]. The Talbot effect has been found plenty of applications in optical metrology [104], imaging processing [126], lithography [56, 114, 72] and data transmission [6]. We consider the Talbot effect manifested in single-photon OAM arrays and the details for our work is described in Chapter 6.

1.4.3 Polarization-OAM Hybrid-entanglement

Hybrid-entanglement is the quantum state entanglement distributed between different degrees of freedoms. Polarization and orbital angular momentum (OAM) are two degrees of freedom of photons for quantum information encoding. Suppose we have a two-photon system Alice (A) and Bob (B), we can create a hybrid-entangled state by combining the two degrees of freedoms for example polarization and OAM together:

$$|\psi_{hybrid}\rangle_{AB} = \frac{1}{\sqrt{2}}\left(|L,0\rangle_A|H,+1\rangle_B + |R,0\rangle_A|H,-1\rangle_B\right) \tag{1.10}$$

where L, R, H represent three polarization and ± 1, 0 stands for OAM degrees of freedoms. This allows for more complex entangled photons states [61, 40] suggesting the various possibilities for quantum correlations encoded in an advanced way spreading among different degrees of freedoms.

Hybrid entanglement is a fascinating resource compared to the normal entanglement and can be employed for the improved versions of quantum information processing protocols. More compatible and efficient quantum communication protocols can also be possible for utilizing these resources.

1.5 Quantum communication protocols

Quantum communication is a quantum information transmission task between two distinct observers realized by two-level physical systems storing quantum information represented by entangled states of qubits [17, 111, 34]. Teleportation and remote state preparation are two major quantum communication protocols.

1.5.1 Teleportation

Quantum teleportation has been a crucial example for quantum communication since it was proposed [13]. It is a task for transporting a quantum state from one place to another.

In quantum teleportation scheme, the sender doesn't know the state $|\psi\rangle$ of the qubit to be communicated. Quantum mechanics doesn't allow it to determine the state as it only has a single copy of the state $|\psi\rangle$. However, quantum teleportation utilizing the entangled EPR state shared between two parties and two classical bits of classical communication instead of sending $|\psi\rangle$ directly to recover the initial copy $|\psi\rangle$ on its remote receiver.

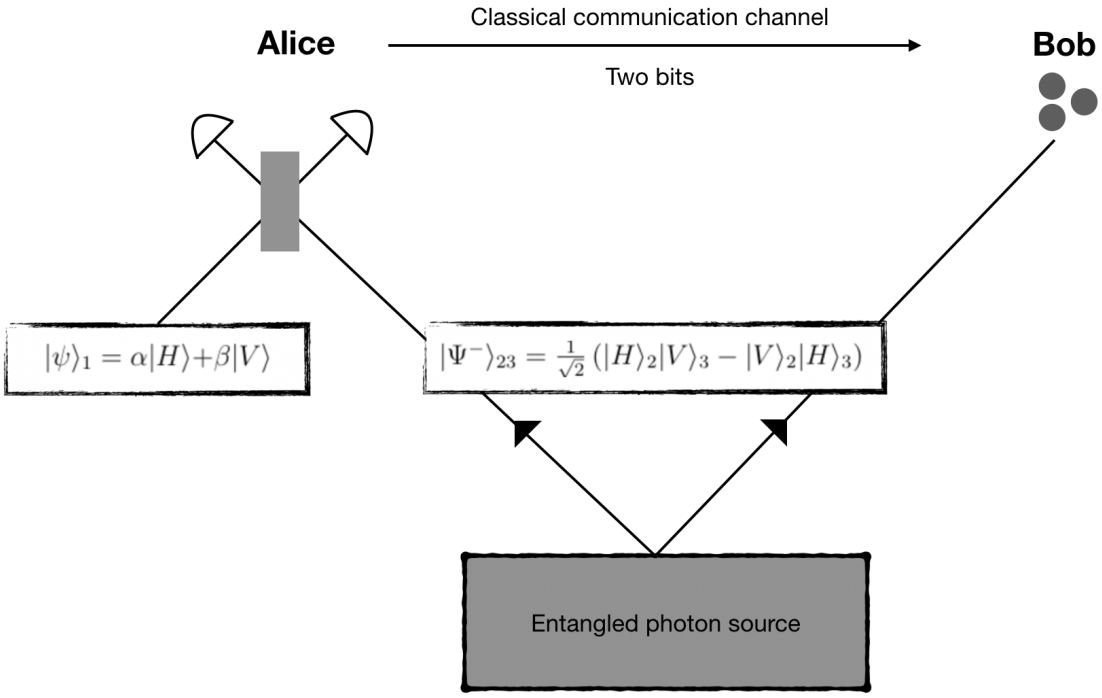

Figure 1.3: Description of teleportation scheme

Here we give an example of quantum teleportation using a photon polarization system as shown in Fig. 1.3. Let's say photon 2 and photon 3 share an entangled state and Alice has an unknown state $|\psi_1\rangle$. The task is to teleport this unknown qubit to Bob, consequently, Bob's photon is reshaped to $|\psi_1\rangle$. So the whole teleportation scheme entails three photons.

In this scheme, the initial entangled states shared by two photons 2 and 3 enables

the quantum channels between these two remote parties Alice and Bob. Typically they share one of the Bell states for example: $|\Psi^-\rangle_{23} = \frac{1}{\sqrt{2}}(|H\rangle_2|V\rangle_3 - |V\rangle_2|H\rangle_3)$. Suppose the photon 1 to be teleported is initially in a state $|\psi\rangle_1 = \alpha|H\rangle + \beta|V\rangle$. Photon 2 and photon 3 are then sent to Alice and Bob respectively. Alice then does a joint Bell measurement on her two particles photon 1 and photon 2 while photon 2 is entangled with photon 3 on Bob side which can be represented as the product of $|\psi\rangle_1$ and $|\Psi^-\rangle_{23}$:

$$\begin{aligned} |\psi\rangle_1|\Psi^-\rangle_{23} = & \frac{1}{2}|\Psi^-\rangle_{12}(\alpha|H\rangle_3 + \beta|V\rangle_3) \\ & + \frac{1}{2}|\Psi^+\rangle_{12}(-\alpha|H\rangle_3 + \beta|V\rangle_3) \\ & + \frac{1}{2}|\Phi^-\rangle_{12}(-\beta|H\rangle_3 + \alpha|V\rangle_3) \\ & + \frac{1}{2}|\Phi^+\rangle_{12}(\beta|H\rangle_3 + \alpha|V\rangle_3) \end{aligned} \tag{1.11}$$

After that Alice can project the states of photon 1 and photon 2 onto one of the four states and then Bob can reshape to the corresponding state of photon 3 immediately. For example, if Alice project the state on $|\Psi^-\rangle_{12}$, then the state of photon 3 at Bob place will be immediately reduced to the state $\alpha|H\rangle_3 + \beta|V\rangle_3$ which is exactly the state of the initial photon 1 on Alice side to be teleported.

1.5.2 Remote state preparation protocol

Remote state preparation (RSP) is a variant of quantum teleportation in which the sender has the complete knowledge of the state to be communicated to its remote receiver [97, 15].

Allowing the sender's knowledge of the transmitted state gives many advantages over the teleportation scheme. To communicate any state in a two-dimensional Hilbert space using quantum state teleportation, one EPR state shared by two parties and two classical bits from a sender are necessary [17]. The task of remotely preparing a specific state can be accomplished with less resources than in the case of teleportation. A maximally entangled state as a shared resource and a single classical bit [74, 95, 70] is sufficient. It is also shown that the knowledge of the prepared state in remote state preparation protocol enables trade-off between entanglement and classical communication resources [15, 16]. Besides quantum teleportation, remote state preparation does not need to perform full Bell-state analysis which currently still be challenging for optical implementation [97].

Two distant parties are involved in remote state preparation protocol, a sender who gives the description of the prepared state $|\psi\rangle$ and the receiver who ideally ends upholding

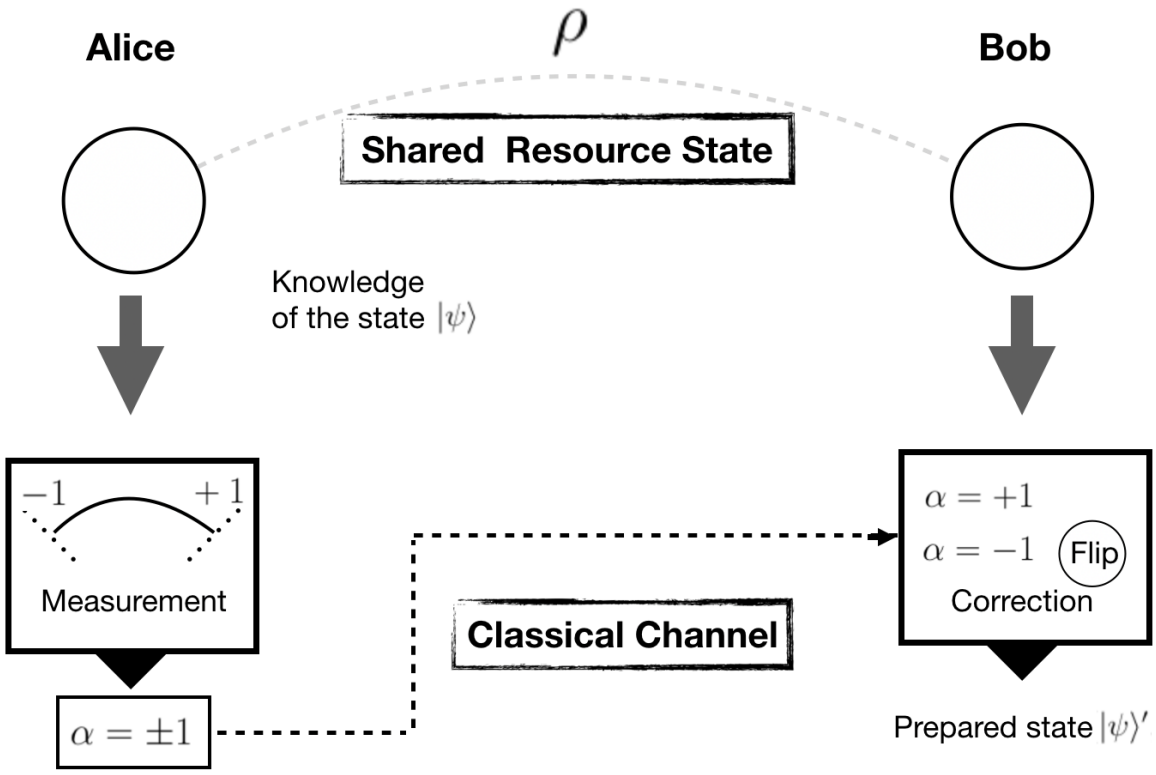

Figure 1.4: Scheme for remote state preparation. Alice and Bob share a quantum state ρ and Alice is able to prepare a state $|\psi\rangle$ in the plane orthogonal to the direction $\boldsymbol{\beta}$. Alice then performs the local measurement and sends the result to Bob through the classical channel. The state $|\psi\rangle'$, which is envisaged by Alice, will be generated on Bob's side after proper correction through decoding channel.

that state based on several resources. The resources can be classical communication, entanglement and shared randomness. It is a process of generating the desired state by a remote observer who merely does a specific measurement locally on his system.

The scheme for the remote state preparation is shown in Fig. 1.4. The sender (Alice) and the receiver (Bob) share a quantum state ρ with various correlations. And Alice uses this shared state to remotely prepare the state $|\psi\rangle$ on the Bob side in the plane that is orthogonal to the direction $\boldsymbol{\beta}$ which is announced by Bob. Alice has the full knowledge about the $|\psi\rangle$ state to be prepared. The state preparation on Bob's side is initialized when

Alice performs a local measurement. Alice's measurement outcome $\alpha = \pm 1$ is then sent to Bob as one classical bit of information along the direction of the state she wants to prepare. Bob will do a state correction based on the value of the received classical bit to obtain the state $|\psi\rangle'$. For example, if $\alpha = -1$, Bob applies a $\pi-$ rotation about $\boldsymbol{\beta}$ to his system and when $\alpha = 1$, Bob applies no correction. The efficiency of the process can be evaluated using a pay-off function $P(|\psi\rangle', |\psi\rangle)$ that is related to the prepared state fidelity.

Take photon polarization as a reference, we consider the two-photon maximally entangled state:

$$|\Phi^+\rangle = \frac{1}{\sqrt{2}}(|H_t H_r\rangle + |V_t V_r\rangle) = \frac{1}{\sqrt{2}}(|D_t D_r\rangle + |A_t A_r\rangle) \tag{1.12}$$

where the subscripts r represents remotely prepared photons and t represents the triggering photon. $|H\rangle$ and $|V\rangle$ stands for horizontal and vertical polarization states, $|D\rangle = \frac{1}{\sqrt{2}}(|H\rangle + |V\rangle)$ and $|A\rangle = \frac{1}{\sqrt{2}}(|H\rangle - |V\rangle)$ stands for diagonal and anti-diagonal polarization respectively. Measuring the trigger photon in diagonal basis ($|D_t\rangle$) prepares the other one in the diagonal state ($|D_r\rangle$).

To remotely prepare an arbitrary pure state $|\psi_r(\theta, \phi)\rangle$ which can be written in $|D\rangle$ and $|A\rangle$ basis as well: $|\psi_r(\theta, \phi)\rangle = \cos\theta|D\rangle + \sin\theta e^{i\phi}|A\rangle$. The sender can act on the triggering photon and with a quarter wave plate and a half wave plate. Thus, the two photon state $|\Phi^+\rangle = \frac{1}{\sqrt{2}}(|D_t\psi_r(\theta, \phi)\rangle + |A_t\psi_r(\theta, \phi)\rangle$ and when the triggering photon is measured in diagonal $|D_t\rangle$, the other remotely prepared photon is in the state $|\psi_r(\theta, \phi)\rangle$. Thus, by projecting the trigger photon into arbitrary polarization with a quarter wave plate and a half wave plate before the polarized beam splitter, we can prepare the other photon into the desired state.

Chapter 2

Source of entangled photons

2.1 Introduction

Both of our experiments need triggered single photons. Especially for the remote state preparation experiment, high quality polarization entangled photon pairs are necessary. In this chapter, I will include a detailed description of how our Sagnac source works, the technique to get high-fidelity polarization entanglement, and the tomography method.

2.2 Layout of the Sagnac source

Our entangled single-photon source is built based on a Sagnac interferometer with two counter-propagating paths on a closed-loop. The set-up of our source is shown in Fig. 2.1. Sagnac interferometer has been largely employed in entangled single-photon sources [38, 66, 65]. The Sagnac entangled single-photon source used in our project was based on the work described in [124].

A 404.4nm Toptica iWave continuous-wave diode laser pump creates correlated photon pairs via a type II SPDC process [52]. By tuning of temperature, the 10 mm long periodically poled potassium titanyl phosphate (PPKTP) nonlinear crystal, degenerated photon pairs (signal and idler) have been generated which enables entangled state with phase matching conditions satisfied.

In Fig. 2.1, we show the set-up for the source. After passing through an optical isolator, the laser is directed to the first half-wave plate (HWP) for setting the polarization of the

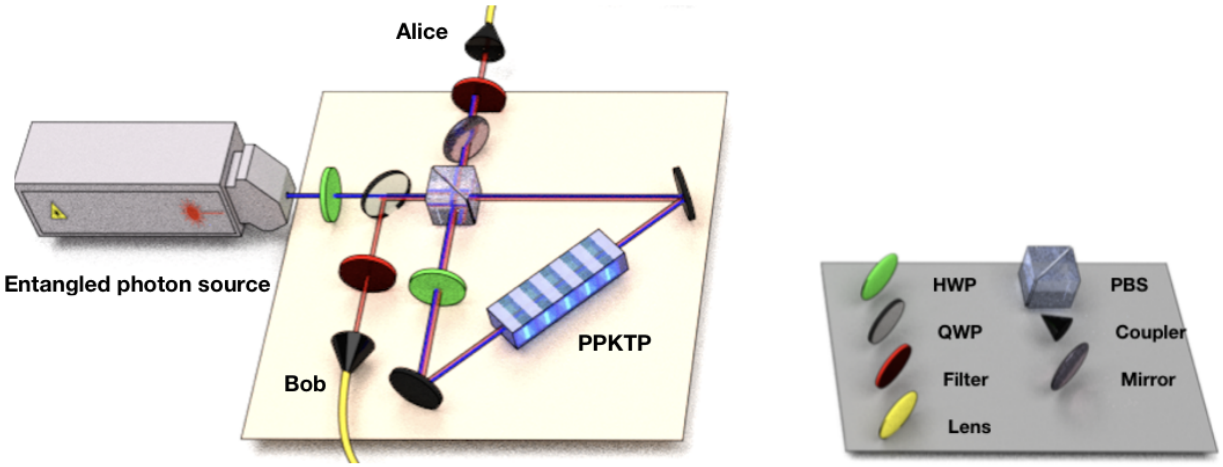

Figure 2.1: Sagnac single-photon source. The highly correlated entangled photon pairs are generated via a type II SPDC process by pumping the diagonally polarized 404.5 nm laser through the Sagnac interferometer. The horizontally polarized photons follow the transmitted path, generating pairs of vertical signal and horizontal idler. The vertically polarized photons follow the reflected path generating pairs of horizontal signal and vertical idler photons.

incoming beam. The light is then directed to a dichroic mirror set at 45 degrees which lets 404.5 nm laser go through while reflecting the down-converted near-infrared photon. The next optical element the laser will encounter is a polarized beam splitter (PBS) which creates two distinguished paths around the Sagnac triangle with two mirrors along the paths. The nonlinear crystal PPKTP is put at the heart of the triangle closed loop. The crystal is set for the type II phase matching, generating the horizontally polarized signal photon and vertically polarized idler photon.

In the Sagnac triangle, The horizontally polarized photons will go through the transmitted path and generate pairs of the vertical signal and horizontal idler photons while the vertically polarized light does the opposite generating pairs of horizontal signal and vertical idler photons. Suppose the incoming light is horizontal, it will transmit through the PBS and takes a clockwise path around the Sagnac triangle. After the type II crystal, horizontal signal and vertical idler photons both at the wavelength of 809 nm are generated. Then photons will pass through the HWP set at 45 degrees, switching their polarization to a vertical signal and a horizontal idler, which will be separated by the PBS again. The ver-

tical signal is reflected when it returns PBS and be reflected again by the dichroic mirror. It is then coupled to the single-mode fiber denoted as Bob's side after an infrared filter filtering out the pump laser. The horizontal idler photon passes through a phase setting tilted QWP and the infrared filter then couples to Alice's side. Similarly, if the polarization of the incoming laser is vertical, it will be reflected anti-clockwise by an HWP (45 degrees) which changes its polarization to horizontal before reaching the nonlinear crystal. It then down converts to a horizontal signal photon and a vertical photon going to Bob and Alice respectively. Since these two photons are indistinguishable, pumping with the equal coherent superposition of horizontal and vertical will create an entangled photon state. Therefore, the diagonally polarized laser should be pumped by setting the first HWP at 22.5 degrees.

To create high fidelity degenerate photons and facilitate the efficient SPDC process, we set the temperature of nonlinear PPKTP crystal to be 75 degrees Celsius. By temperature tuning the type II crystal, we can fine-tune the phase-matching condition. Meeting the phase-matching condition means that the signal and idler photons are created in phase with the pump, giving the best efficiency for SPDC process.

The most common forms of photon entanglement are the four polarization entangled Bell states:

$$|\Phi^{\pm}\rangle = \frac{1}{\sqrt{2}}\left(|H\rangle|H\rangle \pm |V\rangle|V\rangle\right), \quad |\Psi^{\pm}\rangle = \frac{1}{\sqrt{2}}\left(|H\rangle|V\rangle \pm |V\rangle|H\rangle\right) \tag{2.1}$$

These are super-positions of two-qubit polarization state. For instance, the $|\Phi^{+}\rangle$ state which is what we used in our experiment, both photons should be in the same polarization degrees of freedom. By measuring the first photon, the state of the second photon will also be fixed according to the correlations of two photons.

After pumping the diagonally polarized light into the Sagnac interferometer as discussed, we produced the state $|\psi\rangle = |H_i\rangle|V_s\rangle + e^{i\phi}|V_i\rangle|H_s\rangle$ [133, 38]. The phase here can be adjusted by tilting a tilted QWP on Alice's side to get the $|\Psi^{+}\rangle$ bell state. The outputs of photon pairs are then coupled to two single-mode fibers to send them to two parts of the experiments.

By flipping the polarization of Bob using fiber controller, we create the target state $|\Phi^{+}\rangle$ in polarization degree of freedom between two spatially separated parties described in the following formula:

$$|\Phi^{+}\rangle = \frac{1}{\sqrt{2}}\left(|H_{Alice}\rangle|H_{Bob}\rangle + |V_{Alice}\rangle|V_{Bob}\rangle\right) \tag{2.2}$$

To make sure the Sagnac entangled photons source works as we expected, we need to guarantee the alignment of the source is in a good condition before taking data. To aligh the source, we apply the alignment procedures referred to as Hiking Boot and Stiletto in Lydia Vermeyden's Msc thesis [123]. A fidelity of over 97% can be achieved using these techniques.

2.3 Reconstructing the state with quantum state tomography

2.3.1 Introduction to quantum state tomography

Quantum tomography is a method to reconstruct the complete quantum state from a series of experimental measurements on different bases. Quantum state tomography was first introduced by Fano in 1957 [36]. We use the maximum likelihood tomography method to characterize the two-qubit state $|\Phi^+\rangle$ of polarization entanglement.

The density matrix is used for describing the statistical state of a quantum system. It is a general representation for both pure and mixed state, where the mixed state can be defined as a statistical ensemble of pure states. In the case of single-qubit where the density matrix could be written as the linear combination of four Pauli matrices (identity matrix denoted as σ_I plus σ_x, σ_y and σ_z). The two-qubit case can be thought of taking two copies of the single-qubit Hilbert space each representing one of the qubits in the pair. Therefore, the matrix can be spanned by 16 two-qubit Pauli matrices $\sigma_m \otimes \sigma_n (m, n = I, x, y, z)$. Any two-qubit density matrix can be written based on these 16 matrices. However, this representation cannot be adapted to experimental use since we cannot perform all those measurements in the experiment to determine the density matrix. Here we use the maximum estimation to find the density matrix that is compatible with the measurement we can do in the lab. We can get characterize a physical density matrix with the form:

$$\rho = \frac{T^\dagger T}{tr(T^\dagger T)} \tag{2.3}$$

where T is a square matrix and its Hermitian conjugate is $T^\dagger$. From Eq. (2.3), the density matrix is guaranteed to be normalized and positive definite. Since we have 16 independent

real parameters, we can parameterize the matrix T to be:

$$T(t_1, ..., t_{16}) = \begin{bmatrix} t_1 & 0 & 0 & 0 \\ t_5 + it_6 & t_2 & 0 & 0 \\ t_{11} + it_{12} & t_7 + it_8 & t_3 & 0 \\ t_{15} + it_{16} & t_{13} + it_{14} & t_9 + it_{10} & t_4 \end{bmatrix} \tag{2.4}$$

with t_i is real. And if we plug it in the Eq. (2.3), we get the explicit form for the physical density matrix in terms of $T(\vec{t_i})$:

$$\rho = \frac{T(\vec{t_i})^\dagger T(\vec{t_i})}{tr(T(\vec{t_i})^\dagger T(\vec{t_i}))} \tag{2.5}$$

where $\vec{t_i} = (t_1, ..., t_{16})$.

Since our experimental data need to consists of 16 coincidence measurements, n_v and with the expectation values $\langle n_v \rangle = \mathcal{N}\langle \psi_v | \rho | \psi_v \rangle$ where $\mathcal{N}$ is a normalization constant. In terms of the parametrization of the physical density matrix, ρ_p, the expected number of coincidences can be expressed

$$\langle n_v(\vec{t_i}) \rangle = \mathcal{N}\langle \psi_v | \rho_p(\vec{t_i}) | \psi_v \rangle. \tag{2.6}$$

We need a measurement to describe how close our agreement is between the experimental data and reconstructed state. Suppose the coincidence measurements are independent and the presentation of the probability measurement is a Poisson distribution with the mean of n_v, the likelihood function that ρ_p can produce a set of 16 measurements is:

$$\mathcal{L}(\vec{t_i}) = \sum_{v=1}^{16} \langle n_v(\vec{t_i}) \rangle^{n_v} \exp(-\langle n_v(\vec{t_i}) \rangle) \tag{2.7}$$

which is what we are trying to maximize, where the maximum will provide us the most likely set of parameters $\vec{t_i} = (t_1, ..., t_{16})$. We can get the then reconstruct a valid physical matrix using Eq. (2.5) to give the most likely state.

2.3.2 Experimental realization of QST

To reconstruct the state generated by the Sagnac interferometer, and quantify how close it is with the target state between Alice and Bob as described in Eq. (2.2). The experimental

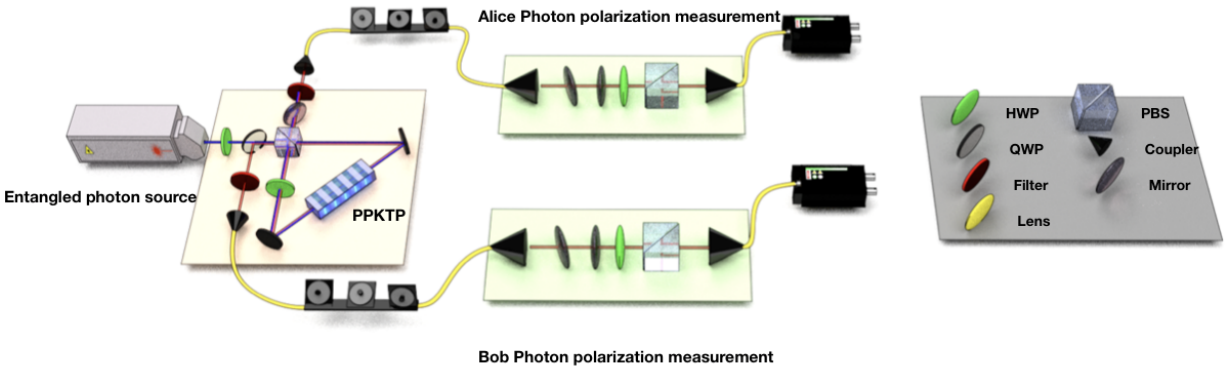

Figure 2.2: Tomography set-up for entangled photons. When a diagonally polarized laser is pumped in the Sagnac photon source, signal photons are coupled to a single-mode fiber to Bob's side while idler photons are coupled to a single-mode fiber to Alice's side. We then do the polarization measurements on both sides for coincidence counts.

set-up for doing state tomography is shown in Fig. 2.2. A quarter-wave plate, a half-wave plate, and a polarization beam splitter are used to make an arbitrary polarization measurement.

We have a pair of wave plates (HWP and QWP) set in each polarization analyzer which projects the prepared state onto the tomographic basis after the PBS. These two sets of wave plate pairs are all motorized and connected to Newport XPS controller which can be controlled by a computer. One photon-counting module is set on each side of the coincidence measurements for full state tomography on the transmitted photons. The coincidence we measure is the event when both detectors detect a certain number of photons within a time window of 3 ns. The "bat ear" and a tilted quarter-wave plate are used for polarization control.

2.3.3 Analysis of the state fidelity

In quantum information theory, the closeness of two quantum states, usually between the measured state and the expected state can be described by the fidelity $\mathcal{F}$ with the definition:

$$\mathcal{F}(\rho_1, \rho_2) = \{tr[(\sqrt{\rho_1}\rho_2\sqrt{\rho_1})^{1/2}]\}^2 \tag{2.8}$$

Maximum Likelihood Matrix

$$\begin{pmatrix} 0.481997 + 1.34416\times10^{-18}\,i & -0.00720864 + 0.0217461\,i & 0.0012813 + 0.0119641\,i & 0.48196 - 0.0515791\,i \\ -0.00720864 - 0.0217461\,i & 0.0108163 + 6.98965\times10^{-19}\,i & 0.00814908 + 0.000359188\,i & -0.0123496 - 0.0218143\,i \\ 0.0012813 - 0.0119641\,i & 0.00814908 - 0.000359188\,i & 0.0109712 + 4.67322\times10^{-19}\,i & -9.35741\times10^{-6} - 0.0104944\,i \\ 0.48196 + 0.0515791\,i & -0.0123496 + 0.0218143\,i & -9.35741\times10^{-6} + 0.0104944\,i & 0.496215 - 2.51045\times10^{-18}\,i \end{pmatrix}$$

Fidelity of measured = 0.971066

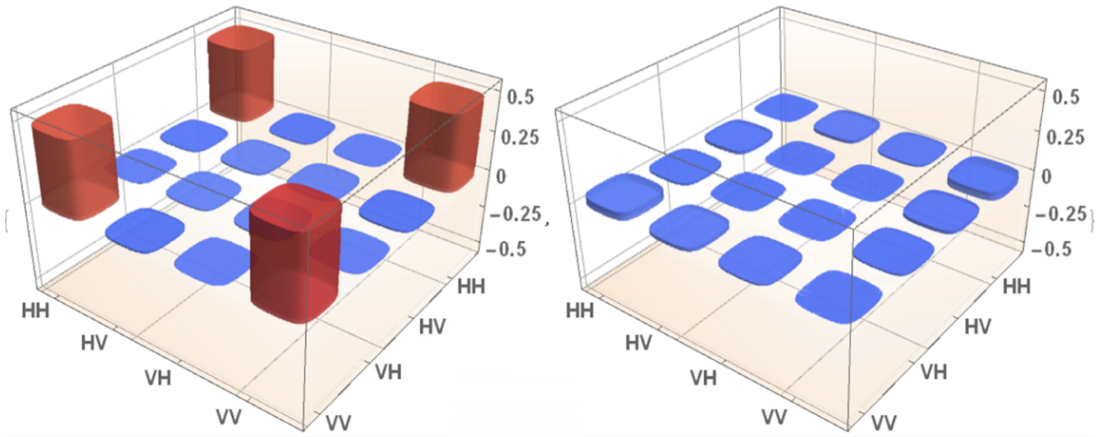

Figure 2.3: Outcome of maximally likelihood tomography. The density matrix is described numerically and the 3D drawing with real part (left) and imaginary (right) part are shown as well. The Mathematica code we use in state tomography is written by previous students Rainer Kaltenbaek and Robert Prevedel in 2010.

where ρ_1 is the reconstructed matrix from experimental measurement, and ρ_2 is the expected $|\Phi^+\rangle\langle\Phi^+|$ density matrix. When $\rho_1 = \rho_2$ we have $\mathcal{F} = 1$ and if ρ_1 is orthogonal to ρ_2 then $\mathcal{F} = 0$. The density matrix is shown both numerically and graphically. The reconstructed matrix's real part (left) and imaginary (right) part is shown in the 3D images as well. We can see the coincidences of $|HH\rangle$ and $|VV\rangle$ are nearly 50% and for other coincidences of different polarization combinations are almost zero. As shown in Fig. 2.3, the fidelity was 97.1% with the Bell state $|\phi^+\rangle$.

Error analysis of the reconstructed density matrices is also necessary. The technique we are using is Monte Carlo simulation, where additional numerically simulated data is used to provide a statistical distribution over the derived quantity. In our case, the two polarization encoded qubits are generated within the ensemble that follows the Poissonian

distribution, and other ensembles can be used to calculate the density matrix using the maximum likelihood technique. In order to define the error, 36 new measurements results are numerically generated, each drawn randomly from the Poissonian distribution with the mean equal to the original ones. These 36 numerically generated results are then fed to the maximum likelihood technique to generate a new density matrix from which we can calculate the tangle which is a measure of the quantum-coherence properties of a quantum state [3]. Thus after one run of this process, a new density matrix and a distribution of tangle are generated which helps determine the error of the original tangle. Additional sets of the simulated data must be generated until the quantity of interest converge to a single value (fluctuation meet the requirement).

Chapter 3

Generation of lattice of spin-orbit coupled state

3.1 Introduction

Spin-orbit coupling enables generation and manipulation of light carrying orbital angular momentum as it utilizes the efficient and well-developed polarization degree of freedom to extend the Hilbert space to a higher dimension. In this chapter, I will introduce an intuitive technique that both of our experiments are based on to generate a lattice of spin-orbit coupled state.

3.2 Optical spin-orbit coupling

Optical spin-orbit coupling is an efficient and powerful way to manipulate the phase and the transverse polarization of the beam via Pancharatnam-Berry phases [105] arising in polarization control. It provides a convenient way to generate and interference orbit angular momentum of single photons with polarization. This is the most widely employed internal degree of freedom to control the quantum state.

The spin is associated with the polarization degree of freedom in the photon system which is independent of the position. Polarization degree of freedom is easy to prepare, control and measure but limited to the two-dimensional system. OAM is associated with the optical wave front induce the revolution of the photon particle around the beam axis.

OAM of photons is a crucial resource for quantum application as it breaks the limitations of quantum information encoding techniques based on the two-dimensional spin angular momentum. Spin and orbital angular momentum seem to be completely separate and no research on spin-induced OAM has taken place for a long time since Allen's paper start the field of OAM [2].

The spin-orbit optical interaction occurs in some appropriately patterned birefringent materials or dichroic media such as "q-plate" [80], spatial light modulator [84], metasurface [137, 77, 62] and Lattice of Optical Vortices (LOV) prism pairs [107]. These enable the spin-orbit quantum transformation of photon states in both polarization space and OAM space. Thus we can prepare the signal photons initially in polarization degrees of freedom to the OAM to explore new possibilities and then transfer the OAM back to the spin space for convenient analysis. There are also works on encoding qubits combining two degrees of freedom through the spin-orbit coupling, trying to encode as much information as possible into one single photon by exploiting different degrees of freedom.

We couple the polarization and OAM using the Lattice of Optical Vortex prism pairs. The following section will give a detailed introduction of the technique we based on [107].

3.3 Lattice of Optical Vortex prism pair

In both experiments demonstrated in Chapter five and Chapter six, we generate a lattice of spin-orbit single-photon states through pairs of linear optical components— Lattice of Optical Vortex prism pairs [107]. This novel technique for generating spin-orbit states uses coherent averaging and spatial control methods to prepare a multiplexing beam consisting of a lattice of OAM states coupled to a two-level system. It gives a two-dimensional control of the length scale of the single lattice cell and also enables customization over azimuthal quantum number l.

3.3.1 Theoretical deduction of LOV prism pairs operator

For the beam carrying OAM, the most important thing is the axis about which the OAM is quantized. The lattice of the OAM beam generated using LOV prism pairs has a two-dimensional array of such axes which are parallel to each other. Here we show what happens within each lattice cell.

The Eq. (3.1) gives the spin-orbit coupling operator [90]:

$$\hat{U} = e^{i\frac{\pi r}{2r_c}[\cos(\phi)\hat{\sigma}_x + \sin(\phi)\hat{\sigma}_y]}, \tag{3.1}$$

expressed in Cartesian coordinates. Here $\sigma_{x,y}$ are Pauli operators and r_c is the length of the smallest radial distance where the polarization degrees of freedom undergo a π rotation. When the radius is not r_c, other rotation angle will occur producing the spin-orbit state :

$$|\psi_{SO}\rangle = \frac{e^{-\frac{r^2}{2}}}{\sqrt{\pi}}[\cos(\frac{\pi r}{2r_c})|L\rangle + \sin(\frac{\pi r}{2r_c})|R\rangle], \tag{3.2}$$

We apply the Suzuki-Trotter expansion to the coupling operator Eq. (3.1) to switch from radial coordinate to Cartesian ones. By proper estimation of this coupling operator, it can be interpreted as a sequence of N perpendicular N-independent linear gradients [107]. In terms of photons, the N independent gradients unit can be produced with the help of optical birefringent prisms pairs which can be described as a combination of two operators defined as $\hat{U}_x$ and $\hat{U}_y$

$$\hat{U}_x = e^{i\frac{\pi}{a}(x-x_0)\hat{\sigma}_x}, \quad \hat{U}_y = e^{i\frac{\pi}{a}(y-y_0)\hat{\sigma}_y}, \tag{3.3}$$

where the origin of the gradients at (x_0, y_0). This equation also shows that if we shift the prism by a distance d along x- or y-axis, there will be a phase shift of $\frac{d\pi}{2r_c}$ occur around the corresponding axis.

The input photons carrying the spin angular momentum only and thus given any polarization input state, N sets of such linear gradients units can prepare a lattice of optical spin-orbit state:

$$|\psi^N_{\text{LOV}}\rangle = (\hat{U}_x\hat{U}_y)^N|\psi_{in(pol)}\rangle \tag{3.4}$$

When we set $N = 2$, it will produce a two dimensional lattice of spin-orbit state with the quantum number of $l = \pm 1$. The birefringence Δn and incline angle θ determine the lattice constant (spacing) a which is two times of the smallest radial distance r_c, as shown in Eq. (3.5):

$$a = 2r_c = \lambda(\Delta n \tan(\theta))^{-1} \tag{3.5}$$

where λ is the wavelength.

After the spin-orbit lattice state is generated after LOV prism pairs, we then post-select on one polarization to yield the distinguishable intensity pattern that can be detected by our single-photon camera. It has been shown that the two coupled states are correlated and post-selection on one degree of freedom will determine the other and reach maximum

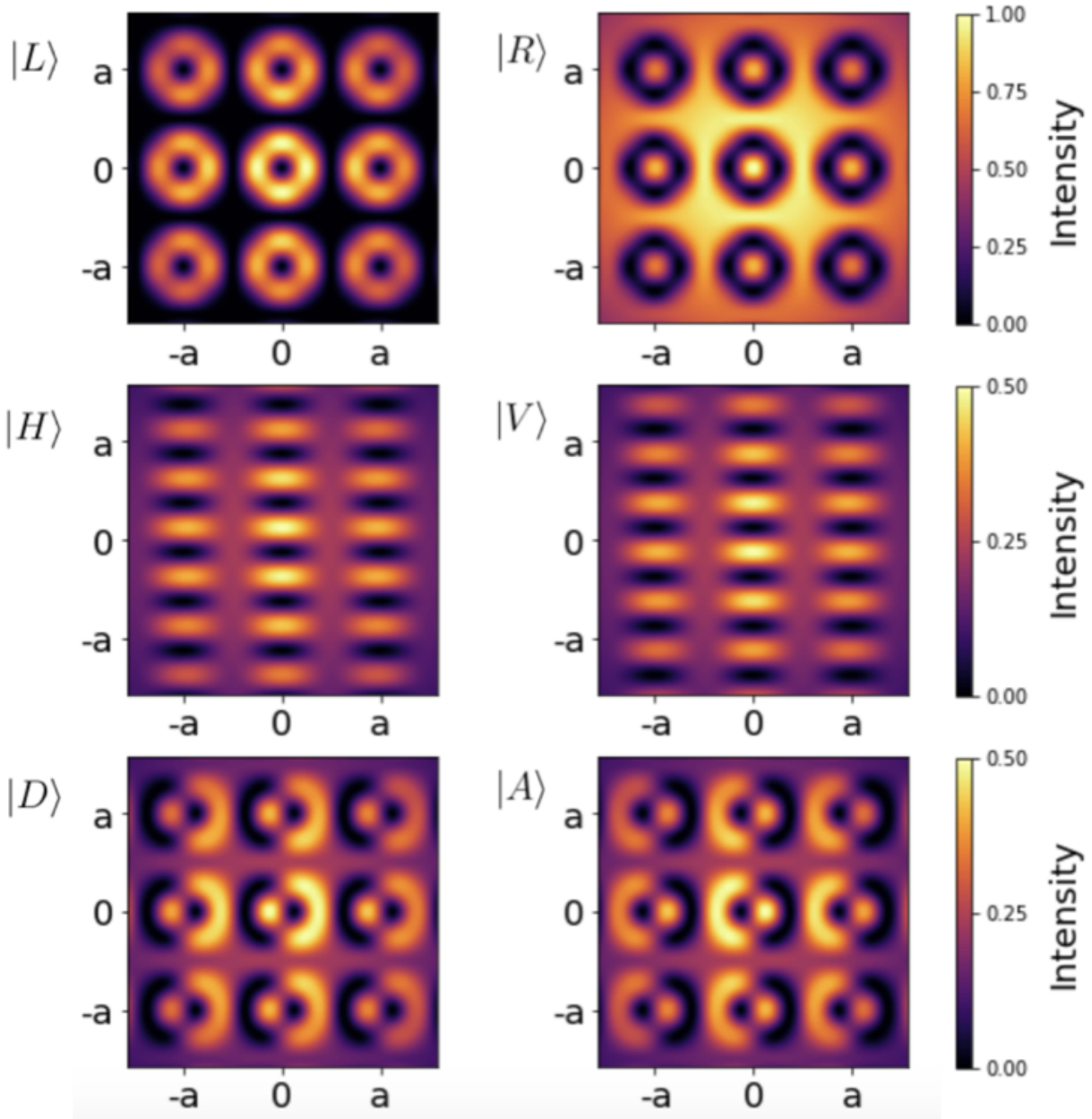

Figure 3.1: Simulated intensity profile of input photons in six polarization bases. The simulation is based on the LOV prism operation code written by Sacha Schwarz in 2018 as shown in Appendix A. The beam waist is set to be 25/3 mm (approximately $3.28a$) which is what we generated in the lab.

correlation when $r_c = 1.82\sigma_\perp$[90]. Finally what we measure is a transverse two-dimensional intensity distribution profile:

$$I_{(P_{Input},P_{Filter})} = |\langle P_{Filter}|(\hat{U}_x\hat{U}_y)^2|P_{Input}\rangle|^2 \tag{3.6}$$

In our scheme, we apply the $N = 2$ sets of linear gradients unit preparing the spin-orbit arrays described in Eq. (3.4) and fix the post-selection polarization to be right circularly polarized $|R\rangle$. Fig. 3.1 shows the simulation for the intensity distribution outcome with six polarization bases of incoming photons: left circular polarization ($|L\rangle$), right circular polarization ($|R\rangle$), horizontal polarization ($|H\rangle$), vertical polarization ($|V\rangle$), diagonal polarization ($|D\rangle$) and anti-diagonal polarization ($|A\rangle$). We can see from the figure that when sending the left circular photons ($|L\rangle$) through $N = 2$ sets of LOV prisms while post-selection on right circular polarization, we get the "ring" like state while getting the opposite "anti-ring" state by sending right circular photons ($|R\rangle$).

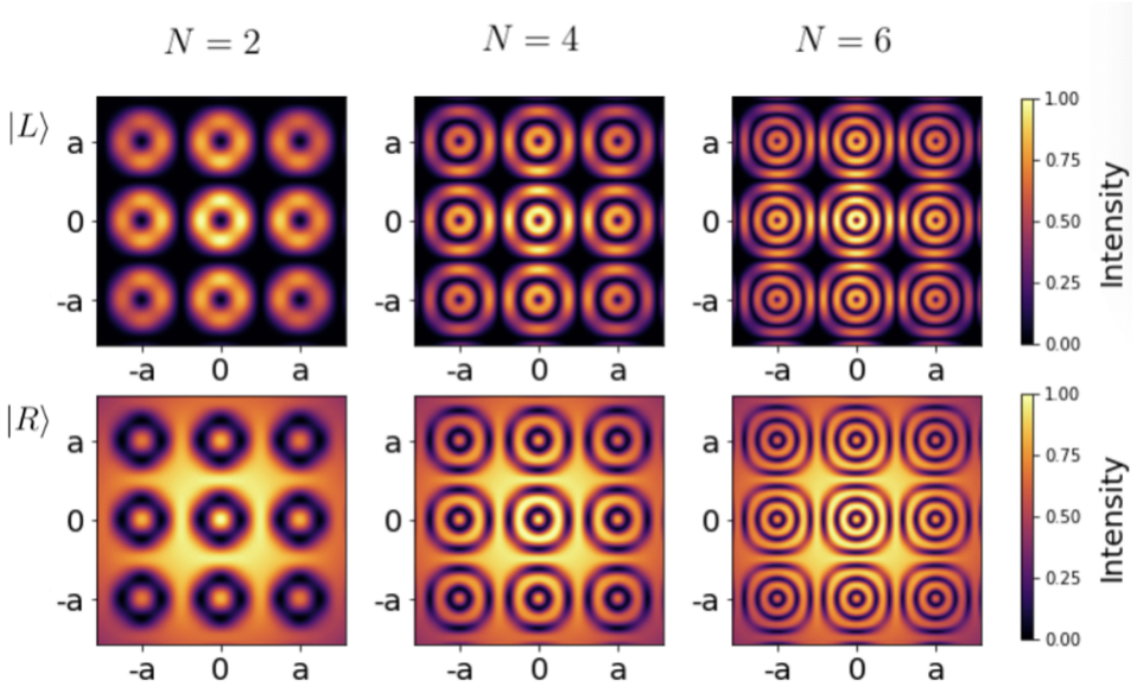

Figure 3.2: Simulated intensity profile $N = 2, 4, 6$ sets of Lattices of Optical Vortex prism pair. The simulation is based on the LOV prism operation code written by Sacha Schwarz in 2018 as shown in Appendix A. The beam waist is set to be $25/3$ mm (approximately $3.28a$) which is what we generated in the lab.

Let's consider the "ring" like state produced by the left circular polarization beam. Suppose we input left circular photons $|L\rangle$ into the N sets of LOV prism pairs. Even if N does not change the phase profile, the number of well-defined rings in each lattice cell increases as we put more prism pairs. In any cell of the arrays, the number of rings is half of the number of LOV prism pairs applied to the initial circularly polarized beam. Thus, N provides control over the mean radial quantum number in the lattice cell. We apply $N = 2$, $N = 4$, $N = 6$ prism configuration individually, Fig. 3.2 shows the simulated intensity distribution patterns "ring" and "anti-ring" states for the $|L\rangle$ and $|R\rangle$ polarization inputs respectively.

3.3.2 Experimental realization

By the preparation of the lattice of spin-orbit state using LOV prism pairs and then filtering the polarization state that is coupled with OAM, we generated a lattice of OAM states. This state coherently couples OAM degrees of freedom of photons with a more easily manipulated spin degree of freedom, offering the possibility for high-dimensional entanglement encoding arbitrary large quanta in principle. The measured structured phase profile reveals the coupling of the polarization degree of freedom to the OAM and is determined by the polarization input to the LOV prism pairs.

One LOV prism pair consists of two perpendicular optical birefringent wedges. The optical axis of the first one is along the prism incline and the second one with an optical axis offset by 45 degrees to give the product operation $\hat{U}_x\hat{U}_y$. The optical axes are represented using the ordinary refractive index n_0 and extraordinary refractive index n_e. We use two sets of such LOV pairs followed by the polarization filter fixed on $|R\rangle$ as shown in Fig. 3.3. The polarization filter is made up of a quarter-wave plate and a polarizing beam splitter.

With the above configuration, we generate a two-dimensional array of OAM states induced by its initial polarization degree of freedom. We can write out the state in each lattice cell as $|\psi_{out}\rangle = \langle R|(\hat{U}_x\hat{U}_y)^2|\psi_{in(pol)}\rangle$ when $|\psi_{in(pol)}\rangle$ state is sent through such setup. The generated lattice constant is determined by the wavelength of the single-photon beam as well as the physical property of the prisms. The photons sent to the LOV prisms are generated from the Sagnac interferometer discussed in Chapter two and are of 810.8 nm wavelength. The prisms used in the LOV pair are made to order by Dmitry Pushin's group. They are made of quartz wedges (bi-refringence of around 0.0091) with a wedge angle θ of 2 degrees and the diameter is 2.54 cm. We can customize the parameters of the prisms to control the lattice constant "a" according to the lattice constant equation Eq. (3.5).

Higher-order OAM structure can be achieved by increasing the above set-up including

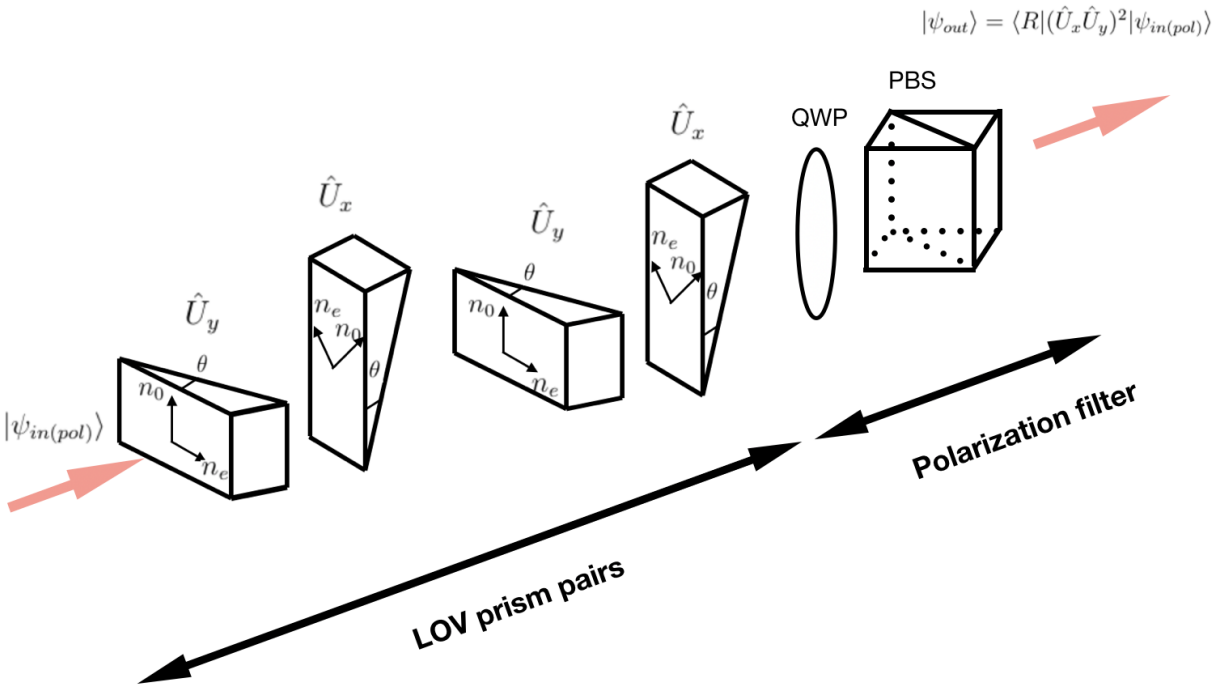

Figure 3.3: $N = 2$ sets of lattices of Optical Vortex

$N = 2$ sets of LOV prism pairs and a polarization filter. Below gives one method for increasing the angular quantum number to m with our LOV prisms:

$$\langle R| \left((\hat{U}_x\hat{U}_y)^2 |R\rangle\langle R| \right)^{m-1} (\hat{U}_x\hat{U}_y)^2 |\psi_{in(pol)}\rangle \tag{3.7}$$

where $|R\rangle\langle R|$ is the operator for polarization filter set in $|R\rangle$. It can be experimentally realized by repeating the unit consisting of a sequence of the $N = 2$ LOV prism pairs followed by a polarization filter shown in Fig. 3.3. This enables coupling polarization state to higher OAM values giving the potential for higher-dimensional quantum space encoded in a single photon.

Chapter 4

EMICCD camera

4.1 Introduction

Modern Intensified CCD cameras can detect single photons and can be triggered in the nanosecond regime. This enables tons of applications in quantum experiments, especially for those involving the spatial modes of photons. In our experiments shown in Chapter 5 and Chapter 6, hybrid-entanglement has been generated. The high-quality intensified CCD camera enables us to observe the quantum entanglement in real-time.

The equipment we use for single-photon detection is the Princeton Instrument $PI - MAX^{®}$ electron-multiplying intensified CCD (emICCD) camera platform.

The present chapter includes a brief introduction of the techniques used in the emICCD camera and its principle of operation for detecting the ultra-weak light such as single photons. Our work on the configuration of controlling software and post-processing to optimize the measurement quality for our purpose will also be discussed.

4.2 Operating principle

The incident photons will first pass through the intensifier input window and hit the photocathode doing the photon-electron transformation and the be electronically magnified when traveling in the image intensifier tube. The image from the image intensifier will be translated to the input of CCD and read out to the internal controller for digitization. The data is then routed to the host computer for processing and display.

4.2.1 Electron-Multiplying gain and Intensifier gain

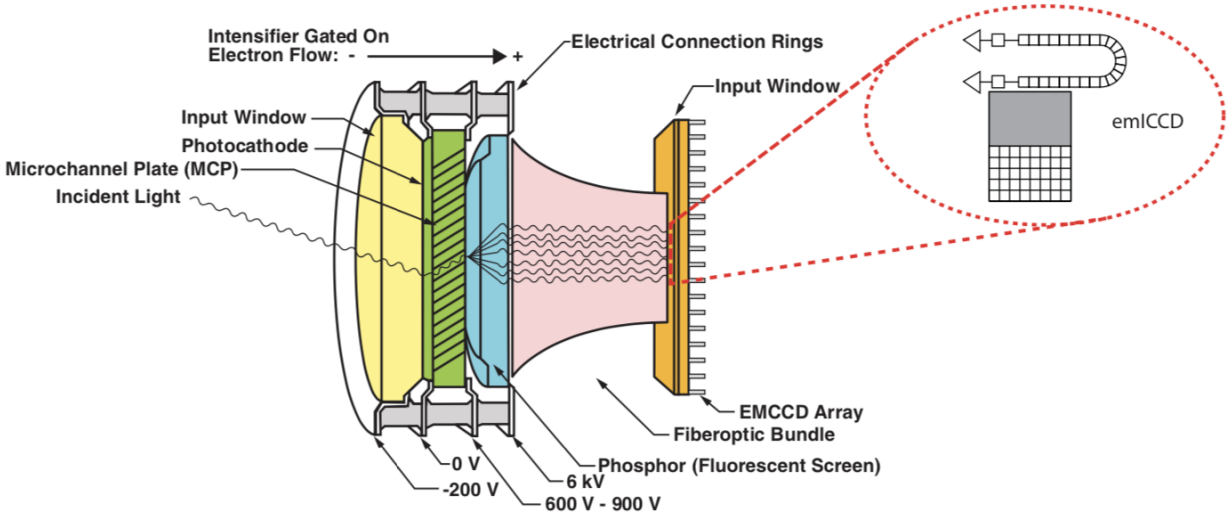

Figure 4.1: emICCD major components

With the advanced emICCD technique, intelligently utilizing the advantages of an intensifier and an electron-multiplying CCD using emICCD mode to obtain < 500 *psec* time resolution, high-quality single-photon detection. The process for the whole signal gain process is shown in the image above Fig. 4.1 [1]. Here we are showing in detail the process of how the incident photons can be converted to the data in the computer which can be used for display and post-processing.

The initial photons will first go through the intensifier tube which is mainly composed of a photocathode, a micro-channel plate (MCP) and a phosphor screen. The principle for controlling the intensifier gain is through changing the photo-cathode voltage concerning the MCP input voltage for switching the intensifier on and off.

The input image of photons is first focused on the photocathode of an image intensifier tube where incident photons are converted to electrons via photo-electric effect. When the intensifier is one where the MCP input is more positive than the photo-cathode, electrons are accelerating to the MCP channel walls which is acted as a distributed electron multiplier, emitting clouds of electrons from every single photo-electron. The amount of gain depends on the voltage of the MCP output. The electrons then get further acceleration by a constant high voltage and hit the phosphor fluorescent screen to transform back to

[1] image come from the PI-MAX4 camera system manual

photons. Now the number of photons released is way more than the incident photons input into the intensifier. The released photons are transferred to the surface of the CCD and keep accumulating the charge produced at each pixel until the intensifier is gated off and the phosphor decays.

Electron Multiplication (EM) is applied as a sensitivity enhancing technique enabling the charge multiplication collected in each pixel of the interested region. Within the array, it will include a second extended serial register where electrons travel with a higher-than-normal CCD clock voltage and the second electron will be generated via the process of impact-ionization within the register. The degree of EM gain can be controlled by the clock voltage applied for the multiplication register. Thus the charge will be shifted to the serial register and the extended EM one where the multiplied electrons can be read out to an on-chip amplifier and convert the charge to the analog voltage, which will then digitized via an analog-to-digital converter. The digitized information will be transmitted from the camera to the host computer stored in RAM which can be display and post-processed.

4.2.2 Data acquisition

Exposure and read-out make up the data acquisition process. Here exposure refers to the integration of the signal on the CCD array and read-out is the transfer of the integrated signal from the array pixels to the shift register and further to the pre-amplifier. Each pixel senses the amount of light falling on its collection area and stores the proportional amount of charge in its well. And once the charge accumulated for the exposure time, which is an important parameter for signal enhancement, it will stop accumulate and read out all the pixels serially.

During the data acquisition process, the image intensifier is gated on and off to allow the pixels to register light during the "on" period and make sure the intensifier is "off" when read-out the pixels. Apart from that, the image intensifier can also greatly brighten our single-photon image. As we mentioned before, the intensifier gain is varied by adjusting the MCP voltage. Exposure is controlled by the gate width and the number of the gates per frame which is the product of these two parameters.

Saturation may occur in the exposure process when the charge generated in one pixel is extremely high and exceed the well capacity, resulting in charge will flow to the adjacent pixels. This is bad for the precision of beam feature capture. When saturation happens, we need to reduce the intensifier gain or the read out more frequently.

After the exposure, the charge from pixels is then transferred to the shift register where the charge is magnified and digitized for data read-out operation. We can choose

the region of interest suitable for our beam size to better the image data. Since the shape of our interested region chosen is always the square fitting the beam signal, dual port readout can be used to accelerate the readout process. During the read-out, the controller gain can be realized on the software setting to change the relation between acquired electron and analog-to-digital generated electron. The analog signal representing the charge of each pixel is digitized and the number of bits per pixel is 16.

4.3 Configuring controlling LightField for taking data

4.3.1 Attempts on noise reduction

Noise reduction is important because the single-photon signal is very weak. Below are the attempts for noise reduction I tried from several aspects.

Before each gated operation, the camera needs to remove the accumulated charge because the camera will acquire the signal no matter whether the gated operation is applied for taking the exposure or not. And even if the data is read out with the intensifier "of" the dark charge will still accumulate and being the only source for single at that time. However, the camera will automatically clean periodically for the dark charge while waiting for acquiring the new data.

However, the noise generated from the power is constant throughout the process. This kind of noise is thermally induced which can be reduced by cooling the CCD array thereby improve the signal to noise ratio. An internal Peltier device directly cools the cold finger which is a piece of laboratory equipment that is used for generating a localized cold surface. The heat can be removed by the air-cooling system enabled by an internal fan and exhausted through the side-panel grill. So it is dangerous to cover the side-panel grill as it will block heart dissipation and may terminate the camera. Supplemental circulating coolant is also provided for further cooling down the camera but it will bring more danger and is not necessary for our condition. By setting the temperature on Light Field (controlling software) to -20 Celsius, the camera will automatically be cooling down the camera to the locked temperature before ready to work. The software will control the cooling circuits of the camera fixed for the set array temperature for stable high-quality measurement.

I also work on reducing the noise light from the lab environment as our emICCD is super sensitive to normal light. By covering the black-out tape on all the possible light sources found in the lab and building a sealed box with a 3 nm narrow-band 808 nm filter to let the signal come in, we reduce the noise from the environment.

Further dark counts reduction is done in the post-processing period and we developed the technique for background subtraction which works well for our measurement and will be discussed later in this chapter.

4.3.2 Gated operation

Gated operation in our emICCD camera behaves like an electronic shutter controlled by the photo-cathode bias making detection of the super weak signals among interfering noise with even higher energy possible. Figuring out how intensifier is being gated to acquire the signal is super important for getting the expected high-quality single-photon intensity pattern.

PI-MAX4 intensifier's photocathode is biased only when the gate pulse is applied. Exposure time is the "on" period when charge integrates on the CCD will get summed to the reported data. Gate width is the time when the light will be detected by the intensifier and applied to the CCD. We can set multiple gates per exposure. Thus for a signal to be detected in the gated intensifier, it needs to fall in a valid gate during a valid exposure time. For a single photon beam, the gate width is usually set at 3 ns which is the same as the coincidence window when doing tomography for a single photon entangled state. The delay time can be set for controlling the time of opening the gate. By calculating the time difference between the triggering photon path and the signaling photon path, we can figure out the time need to be wait is 109 ns in order to capture the correlated photon feature.

We have two valid sources for trigger gating: Internal trigger and External trigger. An internal trigger is just simply counting the signal based on the user-defined internal trigger frequency and it is what we use for a quick check of the signal. For the external triggering mode, it requires an external trigger so our controlling software can record the incoming light when the external triggering signal is recognized at the *Trigger In BNC* on the rear of the camera. For our single-photon beam, the threshold for triggering should is set at 0.5V to better record the incoming single-photon beams on another arm. For the triggering threshold above 1 V like the default one (1.5 V), the triggering photon can't be identified by the camera.

4.3.3 Signal intensity enhancement

The intensifier should be enabled every time we want to acquire the data. Whenever we plan to take data later in the day but don't want to shut down and restart the camera, we can disable the intensifier and keep the measurement environment for safety.

The emICCD gain mode is configured via optimal mode by which we select a value for emICCD gain and the Light Field can then automatically select the best combination of intensifier and EM gain values that provide the best possible signal quality using a complex algorithm. You can also choose the advanced intensifier setting to manually set the intensifier gains and EM gains separately, but is not needed for our purpose.

We can set the Region of Interest and configure the amount of sensor image area used for acquiring the data that fits our beam well. The region we are interested in is only about 150 $pixels \times 150$ $pixels$ out of 1024 $pixels \times 1024$ $pixels$. It is good to every time only take the data in the interested pixel areas because the sensitivity of each pixel might differ from each other. Another benefit from this is that we can accumulate less noise from other pixels and get rid of the interference of irrelevant pixels.

The frame is the area of the CCD array that is readout after an exposure time ends, in our case is the fixed interested area chosen for an incident beam. We set the Frames to Save to 1 as we only want to acquire one image each time for checking when optimizing the parameter settings. Exposure per frame configures whether multiple exposures will occur while a frame is being acquired and On-CCD accumulation is to decide whether multiple frames will be used to create a single frame. These two parameters along with the emICCD gain are the most significant parameters to make the signal intensity up. A good combination of them makes it possible for us to record the super weak single-photon beams with a clear feature we want. Finally, we figure out that the EmICCD Gain at 9000, Exposure Per Frame to 2000, with 50000 On-CCD Accumulation works well and can give us the clear features for measurement with a high signal to noise ratio.

Once we figure out all the parameters configuration for taking single-photon images, make sure the intensifier is on and click the button "acquire" for getting the *csv* version data for later processing. We tested that the configuration of our camera setting parameters works well if the single-photon power is within the valid range (from 10k to 20k single counts). Notice that all the setting we discussed in this chapter is used for the final image, And for the quick check during the parameter optimization process, we can decrease the exposure per frame to 200 saving 10 times as much time.

4.4 Image Post-processing

After getting the original data in a *csv* format, we can process these two-dimensional arrays via background subtraction with adaptive filters. Each CCD has its dark charge pattern or background that can be subtracted directly from the acquired signal image. However; we

want the customized background that has almost the same environment (both the external environment and configuration of emICCD) as our signal frame. In this case, we take noise data of the same frame as the signal data for background subtraction.

Since we want to see the clear feature of the intensity profile with high signal to noise ratio (SNR), our optimization work is based on the feature observed by eye and the SNR calculated as following:

$$S/N = \frac{\overline{Signal}}{\sqrt{Noise}} \tag{4.1}$$

where $\overline{Signal}$ is the mean of the signal frame subtract the mean of the noise frame as Signal and $\sqrt{Noise}$ is the square root the noise counts for the whole frame. Wiener filter is a frequently used signal filter for producing a statistical estimate of an unknown signal with a related signal (Gaussian) by filtering that known signal out. We first apply a Wiener filter on the noise frame with the binning unit of 9 $pixels \times 9$ $pixels$. Binning is a method to associate the countes of one pixels with its nearest neighbour to smooth the image and improve the SNR by summing multiple surrounding pixels together as the count for the center pixel. Then we subtract that filtered noise from the original signal and noise frame and do the second Wiener filter again on both as a new signal frame and noise frame. Using the Eq. (4.1), we calculate the S/N before and after applying filtered background subtraction. We compare the intensity pattern before and after post-processing with SNR as shown in Fig. 4.2.

After that, we apply a non-linear (Gaussian relation with appropriate parameter) color scaling to better distinguish the bright signal point with the dark non-signal point. Also due to the property of the initial Gaussian beam where the intensity decay from the beam center, we divide the signal by a Gaussian to remove the Gaussian profile of the beam. The measurement results shown in Chapter 5 and Chapter 6 are all using the post-processing technique we discuss here.

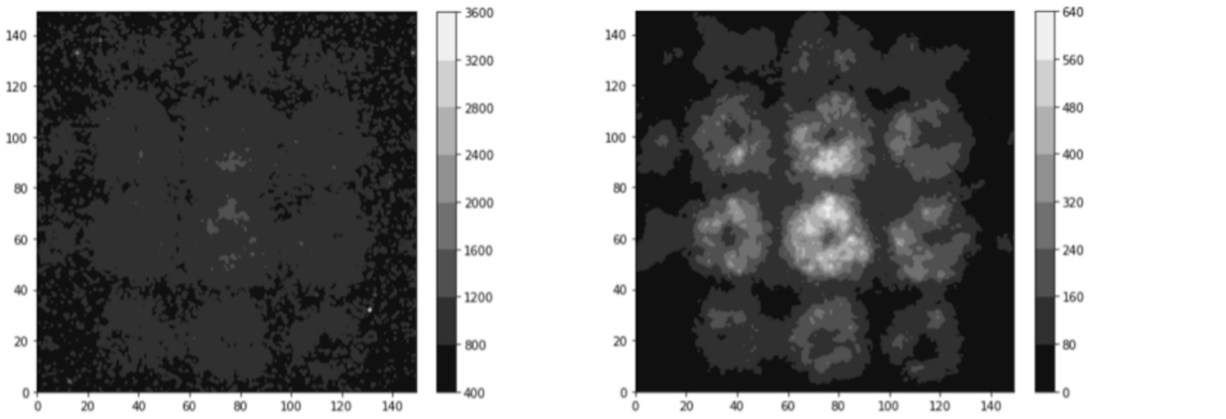

Figure 4.2: Appliance of Post-processing technique

Chapter 5

Remote state preparation with single-photon spin-orbit lattice arrays

Notes and acknowledgements

The contents of this chapter will be published and here are the author contributions to this work:

Kevin Resch and **Dmitry Pushin** conceived of the study.

Ruoxuan Xu, **Andrew Cameron** and **Sacha Schwarz** carried out the experiment.

Connor Kapahi, **Dusan Sarenac**, **Katanya Kuntz** and **Jean-Philippe MacLean** gave guidance in both theoretical and experimental work.

Ruoxuan Xu wrote the first draft of the manuscript.

All author listed above participated in regular discussion throughout the project and contributed to the revision work.

5.1 Introduction

Remote state preparation (RSP) is a quantum communication protocol that relies on the correlation between two distant parties. Here, we implement the remote state preparation in a novel way using hybrid-entanglement. Our RSP scheme can be divided into three

section: generation of the polarization-entangled Bell state $|\Phi^+\rangle$, Spin-orbit transfer on receiver photon using the Lattice of Optical Vortex prism pairs and detection of the prepared state with the emICCD for verifying the state.

5.2 Theory

Starting from the maximally entangled state on polarization degree of freedom created between two remote parties Alice and Bob, the shared entangled resource can be written as

$$|\Phi^+\rangle = \frac{1}{\sqrt{2}} \left(|H_{Alice}\rangle |H_{Bob}\rangle + |V_{Alice}\rangle |V_{Bob}\rangle \right). \tag{5.1}$$

We introduce the spin-orbit coupling on Bob's side can remotely prepare the OAM lattice state by means of linear optic components (LOV) depending on the polarization measurement on Alice's side.

We apply the operator provided by LOV prism pairs given in Eq. (3.3) on Bob's side to generate a lattice of spin-orbit state expressed in Eq. (3.4). In our case, we use $N = 2$ LOV prism pairs configuration shown in Fig. 5.1 and then filter the polarization with respect to $|R\rangle$ to generate two-dimensional arrays which are then coupled with an initial spin degree of freedom with the quantum number of $l = \pm 1$. The number N provides control over the mean radial quantum number in the lattice cell. We can get a higher azimuthal quantum number encoded in a single photon by increasing the LOV prism pairs as shown in Eq. (3.7).

A spin-orbit lattice state is prepared via a remote state preparation protocol. We express the originally generated polarization entangled Bell state $|\Phi^+\rangle$ shown in Eq. (5.1) in the basis of left-handed and right-handed circular polarization states, $|L\rangle$ and $|R\rangle$. One of the photon pair is transferred to the $N = 2$ LOV prism pairs set-up enables the hybrid-entanglement shared between Alice and Bob. The shared state can be rewritten given in Eq. (3.4) for all x and y to

$$\begin{aligned} |\psi_{\text{LOV}}^{N=2}\rangle = & \frac{1}{\sqrt{2}} |+1, P_L\rangle_{Alice} |R\rangle_{Bob} \\ & + \frac{1}{\sqrt{2}} |-1, P_R\rangle_{Alice} |L\rangle_{Bob} \end{aligned} \tag{5.2}$$

where $|+1, P_L\rangle = (\hat{U}_x \hat{U}_y)^2 |0, L\rangle$ and $|-1, P_R\rangle = (\hat{U}_x \hat{U}_y)^2 |0, R\rangle$ are in the basis with OAM quantum number l and polarization P.

It has been shown that the correlation between the coupled spin and orbit degrees of freedom suggests post-selecting on one degree of freedom will determine the other. When Alice performs the polarization measurement, the state $|\psi_{\text{LOV}}\rangle$ collapses and the OAM degrees of freedom yields a transverse field distribution is based on the remotely prepared polarization mixture of Alice and the polarization filtering on Bob side. As a result, what we measure is a transverse two-dimensional intensity distribution as described in Eq. (3.6) $I_{m,n} = |_{Alice}\langle m|_{Bob}\langle n|\psi_{\text{LOV}}\rangle|^2$ when performing m polarization measurement on Alice and filtering Bob with polarization n. We filter the polarization of photons on Bob's side to $|R\rangle$, the measurement on the prepared state we perform on Bob's side can be expressed by $I_m = |_{Alice}\langle m|_{Bob}\langle R|\psi_{\text{LOV}}\rangle|^2$. Thus, the state prepared in Bob's side is only determined by Alice's local polarization measurement m.

5.3 Experimental setup

Our experimental setup is shown in Fig. 5.1. We create a high-fidelity polarization-entangled photon pairs using type II Spontaneous parametric down-conversion (SPDC) by pumping with the 404.4nm Toptica iWave continuous-wave diode laser [52]. By temperature tunning a 10 mm long periodically poled potassium-titanyl-phosphate crystal (PPKTP) at 75 degree celsius, degenerated photon pairs have been generated enabling high-efficiency entanglement.

Pumping with diagonally polarized light into the Sagnac interferometer shown in figure.1, we produced the state $|\psi\rangle = |H_i\rangle|V_s\rangle + e^{i\phi}|V_i\rangle|H_s\rangle$ [133, 38]. The phase can be adjusted by tilting a quarter wave plate on Alice's side to get the $|\Psi^+\rangle$ Bell state. The output of photon pairs are then coupled using single-mode fibers for spatial separation of signal photons (Bob) and idler photons (Alice). By flipping the polarization of Bob using fiber controller, we create a maximally entangled $|\Phi^+\rangle$ state in polarization degree of freedom between two spatially separated photons described in Eq. (5.1) with the fidelity of 97.5% verified by quantum state tomography [124].

We operate on one of the previously entangled photon pairs by sending signal photons to the LOV prism pairs, generating a lattice of spin-orbit states. The signal photon beam is magnified 25/3 times with telescope followed by $N = 2$ sets of LOV prism pairs and a polarization filter fixed on $|R\rangle$ generating the OAM lattice state. In order to display the features of the intensity profile while maintaining the signal to noise ratio, we apply a single-lens imaging system mapping the pattern of prepared state to the sensor of emICCD with a de-magnification factor of 25/6. After the polarization measurement, idler photons are then guided to an avalanche photodiode (APD) which triggers the emICCD offering

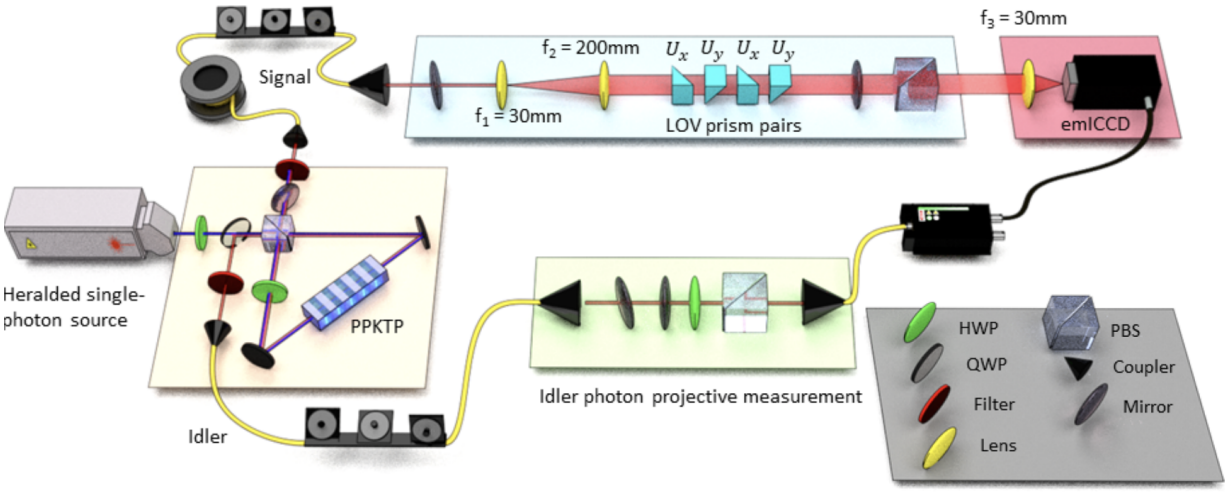

Figure 5.1: Experimental setup for the remote state preparation protocol. Photon pairs are generated via spontaneous parametric down-conversion (SPDC) in a Sagnac interferometer and coupled into single-mode fibers. After the propagation through a 30m long fiber, Bob photon is sent through a telescope with 8x magnification, $N = 2$ sets of LOV prism pairs and a polarization filter. Signal photons are then imaged onto an intensified electron-multiplying CCD (emICCD) triggered by the detection of idler photons. A single-lens imaging system is used for mapping and shrinking the photon beams for better signal to noise ratio.

1 classical bit. Unlike teleportation, we do not require a Bell-state measurement, only a the measurement on signal photons is sufficient.The 30 m single-mode fiber is used for delaying signal photons with respect to the idler photons enabling precise detection of remotely prepared state.

5.4 Results

The measurement of the prepared states is captured by emICCD camera giving a two-dimensional transverse field distribution profile as in Eq. (3.6) for verification of the protocol.

We use the PI-MAX4 Intensified CCD camera (emICCD PI-Max4: 1024 EMB) for acquiring the intensity distribution profile $I(P) = |{}_i\langle P|{}_s\langle R|\psi_{\text{LOV}}\rangle|^2$ where P is the polar-

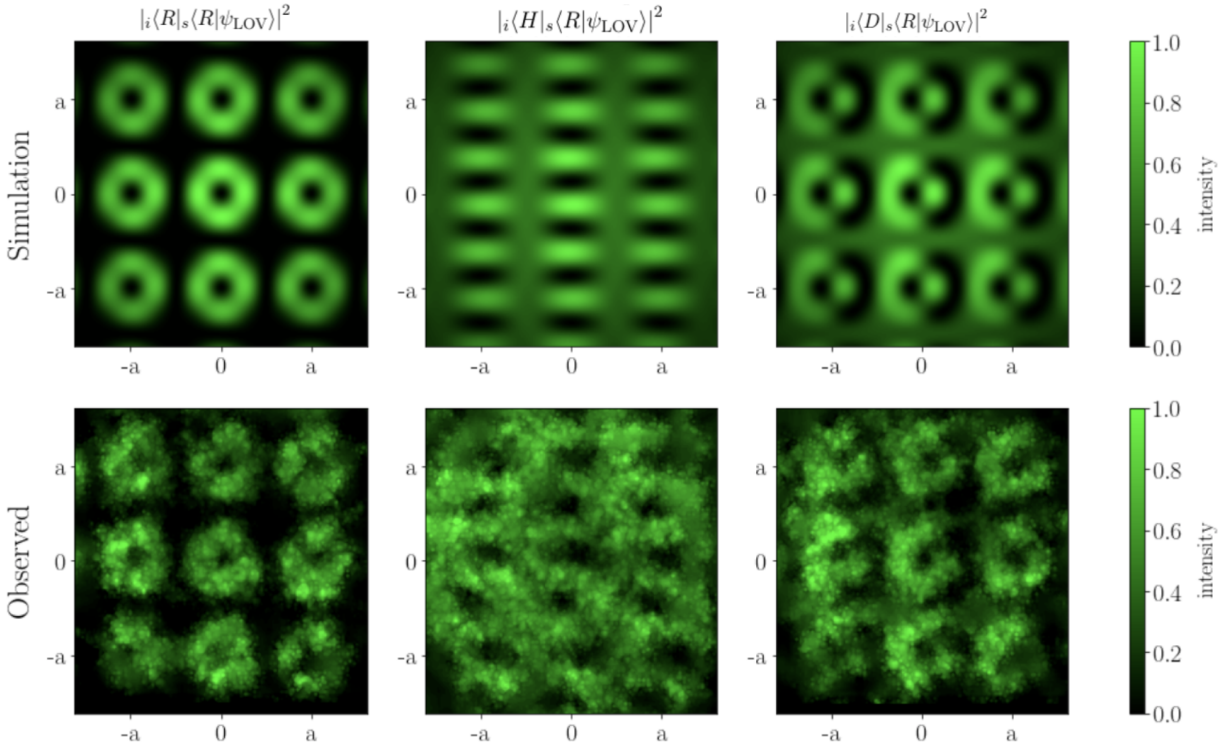

Figure 5.2: Simulated and experimental measurement outcomes for the prepared state. We fix the polarization selection on signal photons after $N = 2$ LOV prism pairs on $|R\rangle$ and measure the two-dimensional intensity distribution $I(P) = |_i\langle P|_s\langle R|\psi_{\mathrm{LOV}}\rangle|^2$ where P is the polarization measurement on idler photons. The measurement taken for the prepared state is determined by the polarization measurement performed on the remote idler photons. Here we show the measurement outcome for prepared state of signal photons by measuring the polarization of idler photons on $|H\rangle$, $|D\rangle$, $|R\rangle$.

ization measurement on idler photons and $|R\rangle$ is the polarization filtered after LOV prism pairs on signal photons. The details for tackling the measurement problem of emICCD camera is discussed in Chapter 4. When the incoming single-photon beam hit the CCD array, the signal photons in interested region (150 pixels by 150 pixels) start to integrate and then be digitalized and transmitted to the computer for storage and display. We use Light-Field as controlling software where we can set the parameter configuration such as *intensity gain*, *exposure per frame*, *on CCD accumulation*. The temperature of the operating environment is fixed at -20 degree Celsius cooling the CCD array for lower dark charge

and further increase the signal to noise ratio. The delay time is set at 109 ns with a 3 ns gate width calculated via traveling time difference between Alice and Bob photon path.

It is shown in Fig. 5.2 that the local polarization measurement on idler photons remotely prepares a OAM lattice state on the other photon. Post-selecting idler photons onto right circular polarization $|R\rangle$ prepares us the lattice of OAM state with a "ring-like" transverse field intensity pattern after filtering on right circular polarization. The "ring-like" state indicates the polarization of signal photons before LOV prism pairs is $|L\rangle$ as shown in the simulation results. This agrees with the correlation of $|R\rangle_{Alice}|L\rangle_{Bob}$ in Bell state $|\Phi^+\rangle$ as shown in Eq. (5.1).

5.5 Conclusion

In this work, we report the demonstration of a remote state preparation protocol with a lattice of spin-orbit single-photon states via hybrid-entanglement. We start with high fidelity polarization entangled state generated by Sagnac single-photon source. By applying an operation on one of the photon pairs via linear optics components demonstrated as LOV prism pairs [107], we prepare lattice of spin-orbit states by performing polarization measurements on its remote photon partner. Our scheme offers high efficiency for remote manipulation of the structured OAM lattice via hybrid-entanglement and has great potential for long-distance compatible and efficient quantum information protocols.

Chapter 6

Talbot effect with single-photon spin-orbit lattice arrays

Notes and acknowledgements

The contents of this chapter has been submitted to publication and here are the author contributions to this work:

Kevin Resch and **Dmitry Pushin** conceived of the study.

Sacha Schwarz, **Ruoxuan Xu** and **Andrew Cameron** carried out the experiment.

Sacha Schwarz performed numerical simulation.

Connor Kapahi, **Dusan Sarenac**, **Katanya Kuntz** and **Jean-Philippe MacLean** gave guidance in both theoretical and experimental work.

Sacha Schwarz wrote the first draft of the manuscript

All author listed above participated in regular discussion throughout the project and contributed to the final version.

6.1 Introduction

The Talbot Effect occurs with the propagation of periodically structured waves and has found its application in optical metrology, image processing, data transmission, and matter-wave interferometer. In this work, we demonstrate the Talbot Effect with a single photon

prepared in a lattice of orbital angular momentum (see Chapter 3). We observe that upon propagation, the wavefronts of the single-photon indicate the periodic helical phase structure which corresponds to a lattice of orbital angular momentum (OAM) state.

6.2 Theory

The Talbot Effect is near-field diffraction where light beams that are periodic in the transverse direction reappear in the propagation direction. We demonstrate the Talbot Effect with single photons prepared in a lattice of orbital angular momentum arrays.

In this work, we focus on the OAM lattice state which is generated using the technique we introduced in Chapter 3. Spin-orbit arrays state can be attained by passing the left circularly polarized light through pairs of LOV prism pairs [107]. Each lattice cell of such beam approximates the following spin-orbit state:

$$|\psi\rangle = A(r,\phi)\left[\cos\left(\frac{\pi r}{d}\right)|L\rangle + ie^{i\ell\phi}\sin\left(\frac{\pi r}{d}\right)|R\rangle\right], \tag{6.1}$$

where (r,ϕ) are the cylindrical coordinates, ℓ specifies the OAM number, d is the distance in which the polarization state performs a full rotation on the Poincaré sphere, $|L\rangle$ and $|R\rangle$ denote the right and left circular polarization states, and $A(r,\phi)$ denotes the envelope. We prepare the lattices of OAM states by filtering the polarization that is coupled with OAM.

The operators of the two perpendicular birefringent gradients are given in Eq. (3.3). Sending a photon in the left circularly polarization state $|L\rangle$ through $N=2$ sets of such prism pairs prepare the state:

$$|\psi_{\mathrm{LOV}}^{N=2}\rangle = \alpha(x,y)(\hat{U}_x\hat{U}_y)^2|L\rangle, \tag{6.2}$$

where $\alpha(x,y)$ describes the incoming Gaussian beam envelope with beam waist w_0. The periodic nature of polarization rotations enables the prism pairs to create a two-dimensional lattice of spin-orbit states.

By filtering the state in Eq. (6.2) on the right circular polarization $|R\rangle$, we obtain the initial intensity distribution profile of the form

$$\begin{aligned} I(x,y) =& |\langle L||\psi_{\mathrm{LOV}}^{N=2}\rangle|^2 \\ =& |\alpha(x,y)|^2\cos^2\left[\frac{\pi x}{a}\right]\cos^2\left[\frac{\pi y}{a}\right] \\ & \times\left(2-\cos\left[\frac{2\pi(x+y)}{a}\right]-\cos\left[\frac{2\pi(x-y)}{a}\right]\right), \end{aligned} \tag{6.3}$$

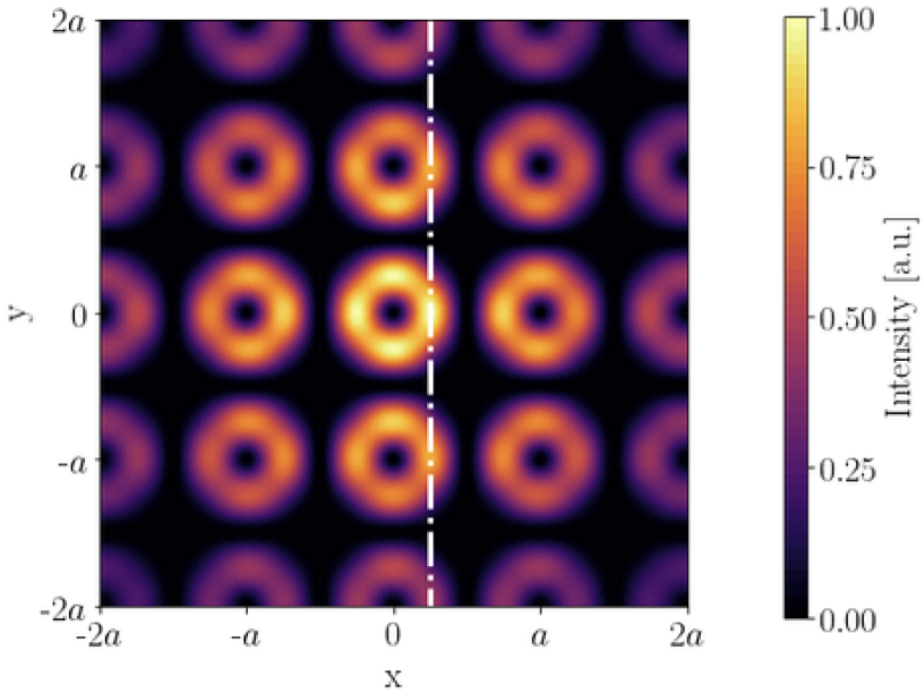

Figure 6.1: Simulated initial distribution in xy plane which is perpendicular to the propagation direction z. This OAM arrays state is obtained by sending left-handed circularly polarized light through $N = 2$ sets of the LOV prism pairs filtered to the right-handed circular polarization at propagation distance $z = 0$.

which is depicted in Fig. 6.1. This periodic beam structure imprinted by the LOV prism pairs sets up conditions required for the Talbot Effect. The transmitted light interferes in such a way that after a Talbot distance expressed in Eq. (1.9), the initial periodic intensity pattern reappears. The same intensity distribution also appears at half the distance, $z_T/2$, but with spatial shifts $\Delta a = a/2$ along the x- and y-directions.

We describe the free-space propagation of single photons by a complex-valued transverse field distribution $E(x, y)$ convoluted with the Fresnel propagator

$$K_F(x, y, z) = \frac{e^{ikz}}{i\lambda z} \exp\left[\frac{ik}{2z}(x^2 + y^2)\right], \tag{6.4}$$

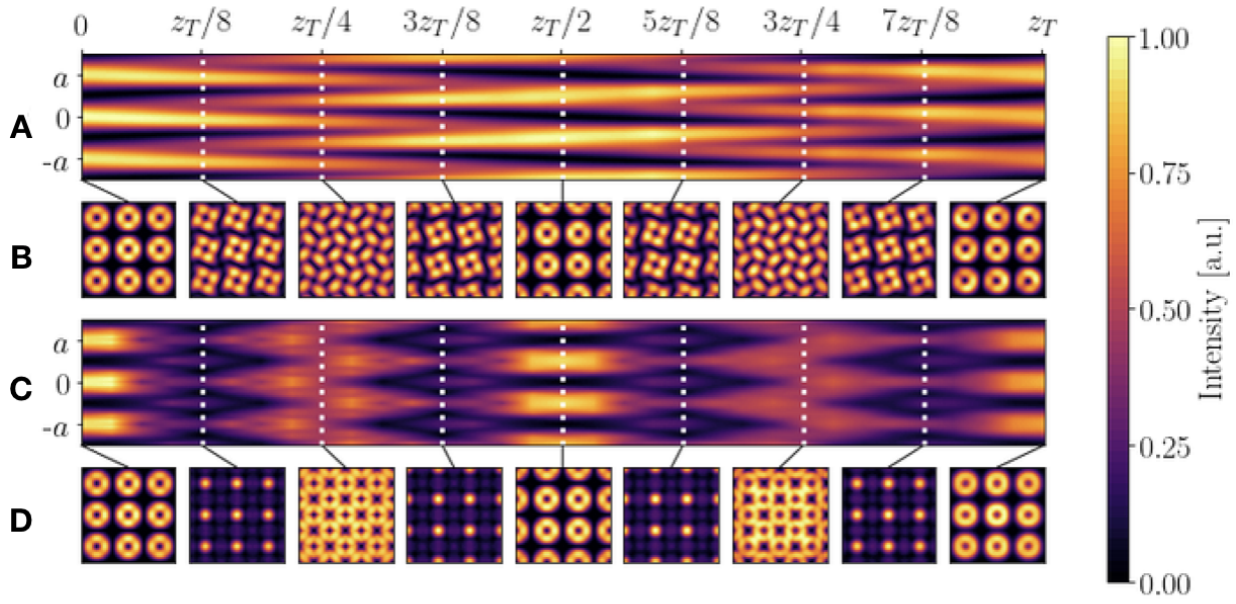

Figure 6.2: (A) By plotting the yz intensity at $x = a/4$ (indicated in Fig. 6.1 with the dash-dotted white line) we recover what is known as the Talbot carpet. (B) xy intensity patterns at specific propagation distances z in (A). (C) The Talbot carpet with no phase structure in the initial beam. (D) the xy intensity cross-sections at certain propagation distance in (C). This demonstrates the effect of the OAM lattice phase structure on the intensity profile at the fractional Talbot Distances.

where k is the wavevector. The field $E(x, y)$ at position z is evaluated via

$$E(x, y, z) = \frac{e^{ikz}}{i\lambda z} \iint dx'dy'\, E(x', y', 0)\, e^{\frac{ik}{2z}[(x-x')^2+(y-y')^2]}. \tag{6.5}$$

In Fig. 6.2, we show the simulated intensity distribution in yz plane when beam propagates along z direction as well as the intensity distribution in xy plane at certain propagation distance. Fig. 6.2 (A) and Fig. 6.2 (C) depict the intensity pattern in yz plane at $x = \frac{1}{4}$ as shown in Fig. 6.1 with a white dash line for the initial intensity profile $\langle L|\psi_{\mathrm{LOV}}^{N=2}\rangle$ and $|\langle L|\psi_{\mathrm{LOV}}^{N=2}\rangle|$, respectively. Fig. 6.2 (B) and Fig. 6.2 (D) give the intensity pattern at certain fractional Talbot distance $z = 0, z_T/8, z_T/4, 3z_T/8, z_T/2, 5z_T/8, 3z_T/4, 7z_T/8, z_T$. Among them, we can also observe that the intensity distributions along the full z_T distance are exactly symmetric about $z = 1/2z_T$.

6.3 Experimental setup

The experimental setup is depicted in Fig. 6.3. We start with degenerated photon pairs generated via type-II spontaneous down-conversion using a Sagnac interferometer (see n Chapter 2). The pump is horizontally polarized creating the target state $|H\rangle_s \otimes |H\rangle_i$ where s stands for signal photon heralded using idler photon denoted as i.

The outputs of the Sagnac interferometer are coupled into two single-mode fibers separating the signal and idler. The signal photons are sent through a telescope to magnify the beam by a factor of 25/3, followed by $N = 2$ sets of LOV prism pairs. This configuration prepares a lattice of spin-orbit states where one of the polarization states is coupled to $\ell = 1$. Higher values of ℓ may be achieved by employing a setup with more LOV prism pairs, while negative values of ℓ may be achieved by changing the input polarization state [107].

The polarization state of the signal photon is prepared using a half-wave plate (HWP) and a quarter-wave plate (QWP). After transmission through the LOV prism pairs, the signal is filtered with respect to left-handed or right-handed circularly polarized light using a QWP. The free-space propagation of the OAM lattice is then analyzed via an arrangement of flip mirrors that effectively change the propagation distance z before measurement. The single-photon detection unit consists of a telescope to demagnify the beam by a factor of 4 (f_3 and f_4 lenses in Fig. 6.3) and a gated intensified electron-multiplying CCD (emICCD PI-Max4: 1024 EMB). The telescope is followed by a single lens (f_5 lens in Fig. 6.3) which images the plane immediately following the telescope.

The idler is detected by an avalanche photodiode, which acts as a trigger for the emICCD, heralding the single-photon state. We use a 30 m spool of single-mode fiber to delay the detection of the signal with respect to the idler to accommodate the delays from triggering electronics. We set the delay time between the idler and signal photon for each propagation distance z and use the emICCD camera to align the coincidence window of 3 ns.

In addition to the single-photon setup, we couple light from a linearly polarized laser diode (central wavelength $\lambda_{LD} = 813.4$ nm) into the signal channel to compare images generated by single photons versus laser diode light. We measure the intensity profile using a conventional CCD camera (Coherent LaserCam-HR II) at the same positions as the single-photon images captured by the emICCD.

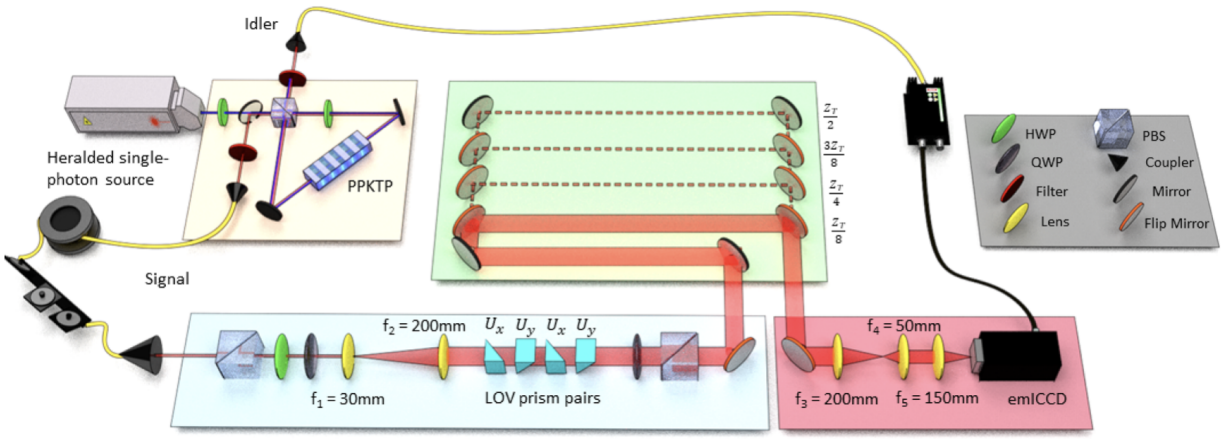

Figure 6.3: Experimental setup for Talbot Effect. Correlated photon pairs are generated via type-II spontaneous parametric down-conversion in a Sagnac interferometer and coupled into single-mode fibers (SMF). A singles rate of 18 kHz and a coincidence rate of 1.5 kHz is measured after the SMF. After propagating through a 30 m long fiber, the signal photon is sent through a telescope with 8.3x magnification, $N = 2$ sets of LOV prism pairs and a polarization filter. The free-space propagation z can be varied via different flip mirror combinations. The signal photons are then imaged onto an intensified electron-multiplying CCD (emICCD), triggered by the detection of the corresponding idler. The imaging arrangement in the detection unit consists of a telescope with 4x demagnification (f_3 and f_4 lenses) followed by a single-lens (f_5) that images the beam onto the detection plane of the emICCD.

6.4 Results

Fig. 6.4 presents the simulated as well as the measured intensity distribution profile using both single-photon and laser diode at fractional Talbot distance $z = 0, z_T/8, z_T/4, 3z_T/8, z_T/2$. In principle the Talbot distance is equal to 16 m.

At half Talbot distance the aperture array repeats itself but with a half-pitch shift from the original structure. Tab. 6.1 lists the experimental distances, Z_{exp}, which effectively correspond to the theoretical distances, Z_{theo}. The observed intensity profiles are processed using background subtraction and an adaptive two-dimensional Gaussian image filter.

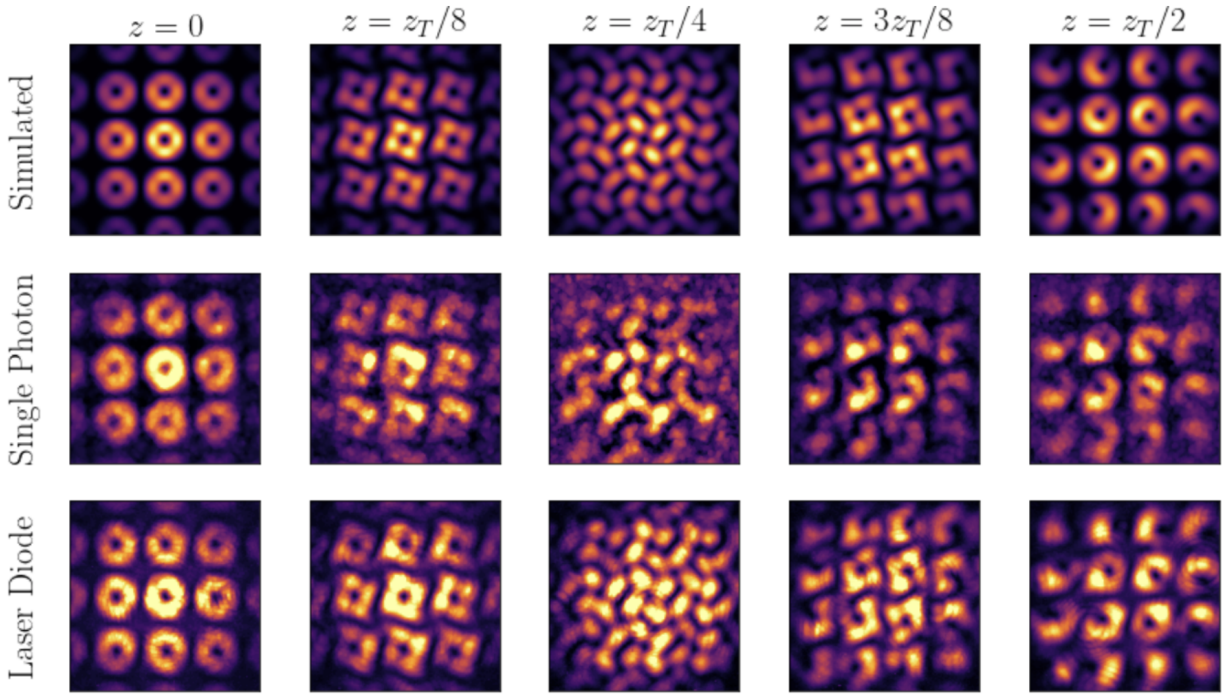

Figure 6.4: Simulated and observed self-images at different fractional Talbot lengths. We measure the two-dimensional intensity profile $I(x, y) = |\langle L|\Psi_{\mathrm{LOV}}^{N=2}\rangle|^2$ at positions $z \in Z_{\mathrm{exp}}$. In the simulation, we multiply a Gaussian beam envelope with the same beam waist w_0 as in the experiment (i.e., $w_0 = (4.1 \pm 0.05)$ mm) to account for features occurring due to finite beams sizes when propagating along the z-axis. For comparison, we couple light from a laser diode into the signal channel, and measure corresponding self-images at the same positions. Good qualitative agreement is found between the simulated and observed profiles.

In Tab. 6.1, we present the SNR before and after the imaging post-processing for different propagation distances. However, it can be noted that the self-imaging property of this beam can be seen clearly in the similarity between images taken at distances $z = \{0, z_T/2\}$, with the correct spatial shift. The propagation distances in the experimental setup were increased by a constant offset of 0.85 m to account for the three lens system in the detection unit [44]. We can see the outermost rings of the $z_T/2$ image are distorted a little bit and that's because of the boundary effect which can be mitigated by using a beam containing more lattice sites.

Z_{theo}	Z_{exp}	Measured SNR	Post-processed SNR
0	0.71 m	0.584	240.377
$z_T/8$	2.86 m	0.547	181.988
$z_T/4$	4.85 m	0.113	102.514
$3z_T/8$	6.87 m	0.159	126.298
$z_T/2$	8.86 m	0.259	264.755

Table 6.1: Experimental propagation distances Z_{exp} which correspond to the fractional Talbot distances Z_{theo}, and single photon signal-to-noise ratio (SNR). The SNR is given by the ratio of the average signal to the standard deviation of the background. In the third (fourth) column, we list the SNR calculated from raw (post-processed) images.

6.5 Conclusion

In this work, we demonstrated and analyzed the Talbot Effect with single photons prepared in a lattice of OAM states. Heralded single photons are sent through $N = 2$ sets of LOV prism pairs and their transverse two-dimensional intensity distributions are measured at various fractional Talbot lengths. The propagation of structured wavefronts is calculated in the near-field and shows good agreement with experimental results. We observe that the initial phase profile defines the transverse intensity pattern at various propagation distances, and thus the Talbot carpet. Future work will scrutinize the connection between OAM and Talbot physics as a new characterization tool. Other avenues of exploration include the addition of path entangled OAM lattices and the implementation of quantum logic using the Talbot Effect and the OAM degree of freedom.

Chapter 7

Summary for the works

The novel method for generating a lattice of spin-orbit beams using Lattice of Optical Vortice (LOV) prism pairs was first demonstrated with neutrons in Dmitry Pushin's group. This method interfaces orbital angular momentum with the easily manipulated spin degree of freedom giving a new possibility for higher dimensional quantum systems. In our work, we repurpose their technique to work with single photons instead of neutrons in order to image the intensity patterns. This also allows us to integrate entanglement into experiment and demonstrate remote state preparation of a novel state.

Photons barely interact with the environment which makes it the most suitable system for long distance quantum communication. Our initial idea was to combine the spin-orbit techniques with quantum entanglement to implement a quantum communication protocol: Remote State Preparation. We begin with high fidelity polarization-entangled photon pairs. By sending one of the photon pairs through two sets of LOV prism pairs followed by a polarization filter, we implement a state preparation scheme between two spatially separated photons sharing a hybrid-entangled state involving polarization and OAM degrees of freedom. We showed that OAM lattice states can be remotely prepared by local polarization projective measurement of its remote partner.

Due to the periodic structure of the OAM lattice we prepared, we can demonstrate a near-field diffraction effect known as the Talbot Effect. The Talbot Effect occurs with the propagation of periodically structured waves. It has enabled several unique applications in optical metrology, image processing, and data transmission. It is a significant addition to the toolbox of orbital angular momentum and spin-orbit techniques which opens another possibility for optical implementations of quantum information.

In order to introduce these two experiments, I first gave a background knowledge in-

troduction in chapter 1 and then discussed in detail the three crucial techniques used in both experiments in chapter 2-4.

Future works for remote state preparation can be finding a method to quantitatively benchmark the entanglement. We can also implement novel high dimensional Quantum Key Distribution protocols that require a structured lattice beam [21]. For the Talbot Effect experiment, we can implement quantum logic with the Talbot Effect of our OAM lattices. Another application we can explore is the phase retrieval of the lattice state using the Talbot Effect with OAM degrees of freedom.

My contributions to these two experiments:

1: Maintained the Sagnac entangled source as shown in Fig. 2.1 which was built by Lydia Vermeyden in 2014;

2: Built the two polarization measurement stages for state tomography, the set-up figure is shown in Fig. 2.2;

3: Implemented the state tomography using vi in Labview and analyzed the reconstructed state using the maximum likelihood Mathematica code written by Rainer Kaltenbaek and Robert Prevedel in 2010;

4: Built the entire experimental set-ups (Fig. 5.1 and Fig. 6.3) for both Remote State Preparation and Talbot Effect experiments with Andrew Cameron and Sacha Schwarz;

5: Fine-tuned the emICCD (software configuration and data post-processing) single-photon camera for good-quality intensity measurements with Connor Kapahi and Andrew Cameron;

6: Wrote the manuscript of the Remote State Preparation experiment.

Other important contributions to these two experiments:

1: Sacha wrote the whole Python package for LOV prism pairs operators;

2: Sacha did the simulations for both set-ups (imaging system, propagation system, etc.) and Talbot Carpet;

3: Sacha wrote the manuscript of the Talbot Effect experiment;

4: Dusan Sarenac and Connor Kapahi helped a lot in controlling the LOV prism;

5: Katanya Kuntz taught Andrew Cameron and me a lot about optics in the lab and did the initial simulation for LOV prism pairs during the first one to two semesters.

References

[1] L Allen, MJ Padgett, and M Babiker. Iv the orbital angular momentum of light. In *Progress in optics*, volume 39, pages 291–372. Elsevier, 1999.

[2] Les Allen, Marco W Beijersbergen, RJC Spreeuw, and JP Woerdman. Orbital angular momentum of light and the transformation of laguerre-gaussian laser modes. *Physical Review A*, 45(11):8185, 1992.

[3] Joseph B Altepeter, Evan R Jeffrey, and Paul G Kwiat. Photonic state tomography. *Advances in Atomic, Molecular, and Optical Physics*, 52:105–159, 2005.

[4] MF Andersen, Changhyun Ryu, Pierre Cladé, Vasant Natarajan, A Vaziri, Kristian Helmerson, and William D Phillips. Quantized rotation of atoms from photons with orbital angular momentum. *Physical review letters*, 97(17):170406, 2006.

[5] Alain Aspect, Philippe Grangier, and Gérard Roger. Experimental realization of einstein-podolsky-rosen-bohm gedankenexperiment: a new violation of bell's inequalities. *Physical review letters*, 49(2):91, 1982.

[6] José Azaña and Miguel A Muriel. Temporal talbot effect in fiber gratings and its applications. *Applied optics*, 38(32):6700–6704, 1999.

[7] R Barboza, U Bortolozzo, G Assanto, E Vidal-Henriquez, MG Clerc, and S Residori. Harnessing optical vortex lattices in nematic liquid crystals. *Physical review letters*, 111(9):093902, 2013.

[8] Adriano Barenco, Charles H Bennett, Richard Cleve, David P DiVincenzo, Norman Margolus, Peter Shor, Tycho Sleator, John A Smolin, and Harald Weinfurter. Elementary gates for quantum computation. *Physical review A*, 52(5):3457, 1995.

[9] Julio T Barreiro, Tzu-Chieh Wei, and Paul G Kwiat. Beating the channel capacity limit for linear photonic superdense coding. *Nature physics*, 4(4):282, 2008.

[10] Stefanie Barz, Ivan Kassal, Martin Ringbauer, Yannick Ole Lipp, Borivoje Dakić, Alán Aspuru-Guzik, and Philip Walther. A two-qubit photonic quantum processor and its application to solving systems of linear equations. *Scientific reports*, 4:6115, 2014.

[11] Wolfgang Becker. *Advanced time-correlated single photon counting techniques*, volume 81. Springer Science & Business Media, 2005.

[12] John S Bell. On the einstein podolsky rosen paradox. *Physics Physique Fizika*, 1(3):195, 1964.

[13] Charles H Bennett, Gilles Brassard, Claude Crépeau, Richard Jozsa, Asher Peres, and William K Wootters. Teleporting an unknown quantum state via dual classical and einstein-podolsky-rosen channels. *Physical review letters*, 70(13):1895, 1993.

[14] Charles H Bennett, Gilles Brassard, Sandu Popescu, Benjamin Schumacher, John A Smolin, and William K Wootters. Purification of noisy entanglement and faithful teleportation via noisy channels. *Physical review letters*, 76(5):722, 1996.

[15] Charles H Bennett, David P DiVincenzo, Peter W Shor, John A Smolin, Barbara M Terhal, and William K Wootters. Remote state preparation. *Physical Review Letters*, 87(7):077902, 2001.

[16] Charles H Bennett, Patrick Hayden, Debbie W Leung, Peter W Shor, and Andreas Winter. Remote preparation of quantum states. *IEEE Transactions on Information Theory*, 51(1):56–74, 2005.

[17] Charles H Bennett and Stephen J Wiesner. Communication via one-and two-particle operators on einstein-podolsky-rosen states. *Physical review letters*, 69(20):2881, 1992.

[18] Gabriel Biener, Avi Niv, Vladimir Kleiner, and Erez Hasman. Formation of helical beams by use of pancharatnam–berry phase optical elements. *Optics letters*, 27(21):1875–1877, 2002.

[19] J-C Boileau, R Laflamme, M Laforest, and CR Myers. Robust quantum communication using a polarization-entangled photon pair. *Physical review letters*, 93(22):220501, 2004.

[20] Danilo Boschi, Salvatore Branca, Francesco De Martini, Lucien Hardy, and Sandu Popescu. Experimental realization of teleporting an unknown pure quantum state

via dual classical and einstein-podolsky-rosen channels. *Physical Review Letters*, 80(6):1121, 1998.

[21] Frédéric Bouchard, Khabat Heshami, Duncan England, Robert Fickler, Robert W Boyd, Berthold-Georg Englert, Luis L Sánchez-Soto, and Ebrahim Karimi. Experimental investigation of high-dimensional quantum key distribution protocols with twisted photons. *arXiv preprint arXiv:1802.05773*, 2018.

[22] Dik Bouwmeester, Jian-Wei Pan, Klaus Mattle, Manfred Eibl, Harald Weinfurter, and Anton Zeilinger. Experimental quantum teleportation. *Nature*, 390(6660):575, 1997.

[23] H-J Briegel, Wolfgang Dür, Juan I Cirac, and Peter Zoller. Quantum repeaters: the role of imperfect local operations in quantum communication. *Physical Review Letters*, 81(26):5932, 1998.

[24] David C Burnham and Donald L Weinberg. Observation of simultaneity in parametric production of optical photon pairs. *Physical Review Letters*, 25(2):84, 1970.

[25] Filippo Cardano, Maria Maffei, Francesco Massa, Bruno Piccirillo, Corrado De Lisio, Giulio De Filippis, Vittorio Cataudella, Enrico Santamato, and Lorenzo Marrucci. Statistical moments of quantum-walk dynamics reveal topological quantum transitions. *Nature communications*, 7:11439, 2016.

[26] Filippo Cardano, Francesco Massa, Hammam Qassim, Ebrahim Karimi, Sergei Slussarenko, Domenico Paparo, Corrado de Lisio, Fabio Sciarrino, Enrico Santamato, Robert W Boyd, et al. Quantum walks and wavepacket dynamics on a lattice with twisted photons. *Science advances*, 1(2):e1500087, 2015.

[27] Michael S Chapman, Christopher R Ekstrom, Troy D Hammond, Jörg Schmiedmayer, Bridget E Tannian, Stefan Wehinger, and David E Pritchard. Near-field imaging of atom diffraction gratings: The atomic talbot effect. *Physical Review A*, 51(1):R14, 1995.

[28] Mario Arnolfo Ciampini, Adeline Orieux, Stefano Paesani, Fabio Sciarrino, Giacomo Corrielli, Andrea Crespi, Roberta Ramponi, Roberto Osellame, and Paolo Mataloni. Path-polarization hyperentangled and cluster states of photons on a chip. *Light: Science & Applications*, 5(4):e16064, 2016.

[29] Domenico D'alessandro and Mohammed Dahleh. Optimal control of two-level quantum systems. *IEEE Transactions on Automatic Control*, 46(6):866–876, 2001.

[30] Sarayut Deachapunya, Sorakrai Srisuphaphon, Pituk Panthong, Thanarwut Photia, Kitisak Boonkham, and Surasak Chiangga. Realization of the single photon talbot effect with a spatial light modulator. *Optics express*, 24(18):20029–20035, 2016.

[31] Lu Deng, Edward W Hagley, J Denschlag, JE Simsarian, Mark Edwards, Charles W Clark, Kristian Helmerson, SL Rolston, and William D Phillips. Temporal, matter-wave-dispersion talbot effect. *Physical Review Letters*, 83(26):5407, 1999.

[32] K Dholakia and T Čižmár. Shaping the future of manipulation. *Nature photonics*, 5(6):335, 2011.

[33] L-M Duan and HJ Kimble. Scalable photonic quantum computation through cavity-assisted interactions. *Physical review letters*, 92(12):127902, 2004.

[34] L-M Duan, MD Lukin, J Ignacio Cirac, and Peter Zoller. Long-distance quantum communication with atomic ensembles and linear optics. *Nature*, 414(6862):413, 2001.

[35] Albert Einstein, Boris Podolsky, and Nathan Rosen. Can quantum-mechanical description of physical reality be considered complete? *Physical review*, 47(10):777, 1935.

[36] Ugo Fano. Description of states in quantum mechanics by density matrix and operator techniques. *Reviews of Modern Physics*, 29(1):74, 1957.

[37] Osvaldo Jiménez Farías, Fernando de Melo, Perola Milman, and Stephen P Walborn. Quantum information processing by weaving quantum talbot carpets. *Physical Review A*, 91(6):062328, 2015.

[38] Alessandro Fedrizzi, Thomas Herbst, Andreas Poppe, Thomas Jennewein, and Anton Zeilinger. A wavelength-tunable fiber-coupled source of narrowband entangled photons. *Optics Express*, 15(23):15377–15386, 2007.

[39] Robert Fickler, Radek Lapkiewicz, William N Plick, Mario Krenn, Christoph Schaeff, Sven Ramelow, and Anton Zeilinger. Quantum entanglement of high angular momenta. *Science*, 338(6107):640–643, 2012.

[40] Robert Fickler, Radek Lapkiewicz, Sven Ramelow, and Anton Zeilinger. Quantum entanglement of complex photon polarization patterns in vector beams. *Physical Review A*, 89(6):060301, 2014.

[41] Fulvio Flamini, Nicolò Spagnolo, and Fabio Sciarrino. Photonic quantum information processing: a review. *Reports on Progress in Physics*, 82(1):016001, 2018.

[42] Stuart J Freedman and John F Clauser. Experimental test of local hidden-variable theories. *Physical Review Letters*, 28(14):938, 1972.

[43] Tingge Gao, E Estrecho, G Li, Oleg A Egorov, X Ma, Karol Winkler, Martin Kamp, C Schneider, Sven Hoefling, AG Truscott, et al. Talbot effect for exciton polaritons. *Physical review letters*, 117(9):097403, 2016.

[44] Joseph W Goodman. *Introduction to Fourier optics*. Roberts and Company Publishers, 2005.

[45] Trent M Graham, Herbert J Bernstein, Tzu-Chieh Wei, Marius Junge, and Paul G Kwiat. Superdense teleportation using hyperentangled photons. *Nature communications*, 6:7185, 2015.

[46] Simon Gröblacher, Thomas Jennewein, Alipasha Vaziri, Gregor Weihs, and Anton Zeilinger. Experimental quantum cryptography with qutrits. *New Journal of Physics*, 8(5):75, 2006.

[47] Lov K Grover. A fast quantum mechanical algorithm for database search. *arXiv preprint quant-ph/9605043*, 1996.

[48] Mark T Gruneisen, Raymond C Dymale, Kurt E Stoltenberg, and Nicholas Steinhoff. Optical vortex discrimination with a transmission volume hologram. *New Journal of Physics*, 13(8):083030, 2011.

[49] E Hagley, X Maitre, G Nogues, C Wunderlich, M Brune, Jean-Michel Raimond, and Serge Haroche. Generation of einstein-podolsky-rosen pairs of atoms. *Physical Review Letters*, 79(1):1, 1997.

[50] Davit Hakobyan and Etienne Brasselet. Left-handed optical radiation torque. *Nature Photonics*, 8(8):610, 2014.

[51] H He, MEJ Friese, NR Heckenberg, and H Rubinsztein-Dunlop. Direct observation of transfer of angular momentum to absorptive particles from a laser beam with a phase singularity. *Physical review letters*, 75(5):826, 1995.

[52] CK Hong and L Mandel. Theory of parametric frequency down conversion of light. *Physical Review A*, 31(4):2409, 1985.

[53] Ryszard Horodecki, Paweł Horodecki, Michał Horodecki, and Karol Horodecki. Quantum entanglement. *Reviews of modern physics*, 81(2):865, 2009.

[54] John C Howell, Ryan S Bennink, Sean J Bentley, and RW Boyd. Realization of the einstein-podolsky-rosen paradox using momentum-and position-entangled photons from spontaneous parametric down conversion. *Physical Review Letters*, 92(21):210403, 2004.

[55] A Imamog, David D Awschalom, Guido Burkard, David P DiVincenzo, Daniel Loss, M Sherwin, A Small, et al. Quantum information processing using quantum dot spins and cavity qed. *Physical review letters*, 83(20):4204, 1999.

[56] A Isoyan, F Jiang, YC Cheng, F Cerrina, P Wachulak, L Urbanski, J Rocca, C Menoni, and M Marconi. Talbot lithography: self-imaging of complex structures. *Journal of Vacuum Science & Technology B: Microelectronics and Nanometer Structures Processing, Measurement, and Phenomena*, 27(6):2931–2937, 2009.

[57] Barry Jack, P Aursand, S Franke-Arnold, David G Ireland, Jonathan Leach, Stephen M Barnett, and Miles J Padgett. Demonstration of the angular uncertainty principle for single photons. *Journal of Optics*, 13(6):064017, 2011.

[58] Thomas Jennewein, Christoph Simon, Gregor Weihs, Harald Weinfurter, and Anton Zeilinger. Quantum cryptography with entangled photons. *Physical Review Letters*, 84(20):4729, 2000.

[59] Richard Jozsa and Noah Linden. On the role of entanglement in quantum-computational speed-up. *Proceedings of the Royal Society of London. Series A: Mathematical, Physical and Engineering Sciences*, 459(2036):2011–2032, 2003.

[60] Rainer Kaltenbaek, Markus Aspelmeyer, Thomas Jennewein, Caslav Brukner, Anton Zeilinger, Martin Pfennigbauer, and Walter R Leeb. Proof-of-concept experiments for quantum physics in space. In *Quantum Communications and Quantum Imaging*, volume 5161, pages 252–268. International Society for Optics and Photonics, 2004.

[61] Ebrahim Karimi, Jonathan Leach, Sergei Slussarenko, Bruno Piccirillo, Lorenzo Marrucci, Lixiang Chen, Weilong She, Sonja Franke-Arnold, Miles J Padgett, and Enrico Santamato. Spin-orbit hybrid entanglement of photons and quantum contextuality. *Physical review A*, 82(2):022115, 2010.

[62] Ebrahim Karimi, Sebastian A Schulz, Israel De Leon, Hammam Qassim, Jeremy Upham, and Robert W Boyd. Generating optical orbital angular momentum at

visible wavelengths using a plasmonic metasurface. *Light: Science & Applications*, 3(5):e167, 2014.

[63] Inge C Kerssens-Van Drongelen, Petra C De Weerd-Nederhof, and Olaf AM Fisscher. Describing the issues of knowledge management in r&d: towards a communication and analysis tool. *R&D Management*, 26(3):213–230, 1996.

[64] Sergei Ya Kilin. Quantum information. *Physics-Uspekhi*, 42(5):435, 1999.

[65] Taehyun Kim, Marco Fiorentino, and Franco NC Wong. Phase-stable source of polarization-entangled photons using a polarization sagnac interferometer. *Physical Review A*, 73(1):012316, 2006.

[66] Onur Kuzucu and Franco NC Wong. Pulsed sagnac source of narrow-band polarization-entangled photons. *Physical Review A*, 77(3):032314, 2008.

[67] Paul G Kwiat, Klaus Mattle, Harald Weinfurter, Anton Zeilinger, Alexander V Sergienko, and Yanhua Shih. New high-intensity source of polarization-entangled photon pairs. *Physical Review Letters*, 75(24):4337, 1995.

[68] Paul G Kwiat, Aephraim M Steinberg, and Raymond Y Chiao. High-visibility interference in a bell-inequality experiment for energy and time. *Physical Review A*, 47(4):R2472, 1993.

[69] R Laflamme, E Knill, DG Cory, EM Fortunato, T Havel, C Miquel, R Martinez, C Negrevergne, G Ortiz, MA Pravia, et al. Introduction to nmr quantum information processing. *arXiv preprint quant-ph/0207172*, 2002.

[70] Debbie W Leung and Peter W Shor. Oblivious remote state preparation. *Physical review letters*, 90(12):127905, 2003.

[71] Jun Liu, Shi-Mao Li, Long Zhu, An-Dong Wang, Shi Chen, Charalambos Klitis, Cheng Du, Qi Mo, Marc Sorel, Si-Yuan Yu, et al. Direct fiber vector eigenmode multiplexing transmission seeded by integrated optical vortex emitters. *Light: Science & Applications*, 7(3):17148, 2018.

[72] Yingying Liu, Xing Zhang, Youwen Huang, Jianwei Zhang, Werner Hofmann, Yongqiang Ning, and Lijun Wang. Polarization stabilized vcsels by displacement talbot lithography-defined surface gratings. *Optik*, 183:579–585, 2019.

[73] Seth Lloyd. Universal quantum simulators. *Science*, pages 1073–1078, 1996.

[74] Hoi-Kwong Lo. Classical-communication cost in distributed quantum-information processing: a generalization of quantum-communication complexity. *Physical Review A*, 62(1):012313, 2000.

[75] Hoi-Kwong Lo and Hoi Fung Chau. Unconditional security of quantum key distribution over arbitrarily long distances. *science*, 283(5410):2050–2056, 1999.

[76] Chaoxuan Ma, Wesley D Sacher, Zhiyuan Tang, Jared C Mikkelsen, Yisu Yang, Feihu Xu, Torrey Thiessen, Hoi-Kwong Lo, and Joyce KS Poon. Silicon photonic transmitter for polarization-encoded quantum key distribution. *Optica*, 3(11):1274–1278, 2016.

[77] Xiaoliang Ma, Mingbo Pu, Xiong Li, Cheng Huang, Yanqin Wang, Wenbo Pan, Bo Zhao, Jianhua Cui, Changtao Wang, ZeYu Zhao, et al. A planar chiral metasurface for optical vortex generation and focusing. *Scientific reports*, 5:10365, 2015.

[78] Alois Mair, Alipasha Vaziri, Gregor Weihs, and Anton Zeilinger. Entanglement of the orbital angular momentum states of photons. *Nature*, 412(6844):313, 2001.

[79] Vasiliy Makhalov and Andrey Turlapov. Order in the interference of a long chain of bose condensates with unrestricted phases. *Physical review letters*, 122(9):090403, 2019.

[80] Lorenzo Marrucci, C Manzo, and D Paparo. Optical spin-to-orbital angular momentum conversion in inhomogeneous anisotropic media. *Physical review letters*, 96(16):163905, 2006.

[81] Jonathan CF Matthews, Alberto Politi, Damien Bonneau, and Jeremy L OBrien. Heralding two-photon and four-photon path entanglement on a chip. *Physical review letters*, 107(16):163602, 2011.

[82] Jonathan CF Matthews, Konstantinos Poulios, Jasmin DA Meinecke, Alberto Politi, Alberto Peruzzo, Nur Ismail, Kerstin Wörhoff, Mark G Thompson, and Jeremy L O'brien. Observing fermionic statistics with photons in arbitrary processes. *Scientific reports*, 3:1539, 2013.

[83] Klaus Mattle, Harald Weinfurter, Paul G Kwiat, and Anton Zeilinger. Dense coding in experimental quantum communication. *Physical Review Letters*, 76(25):4656, 1996.

[84] Christian Maurer, Alexander Jesacher, Severin Fürhapter, Stefan Bernet, and Monika Ritsch-Marte. Tailoring of arbitrary optical vector beams. *New Journal of Physics*, 9(3):78, 2007.

[85] Gabriel Molina-Terriza, Juan P Torres, and Lluis Torner. Twisted photons. *Nature physics*, 3(5):305, 2007.

[86] Eleonora Nagali, Linda Sansoni, Lorenzo Marrucci, Enrico Santamato, and Fabio Sciarrino. Experimental generation and characterization of single-photon hybrid ququarts based on polarization and orbital angular momentum encoding. *Physical Review A*, 81(5):052317, 2010.

[87] DS Naik, CG Peterson, AG White, AJ Berglund, and P_ G Kwiat. Entangled state quantum cryptography: eavesdropping on the ekert protocol. *Physical Review Letters*, 84(20):4733, 2000.

[88] Sebastian Nauerth, Florian Moll, Markus Rau, Christian Fuchs, Joachim Horwath, Stefan Frick, and Harald Weinfurter. Air-to-ground quantum communication. *Nature Photonics*, 7(5):382, 2013.

[89] Michael A Nielsen and Isaac Chuang. Quantum computation and quantum information, 2002.

[90] Joachim Nsofini, Dusan Sarenac, Christopher J Wood, David G Cory, Muhammad Arif, Charles W Clark, Michael G Huber, and Dmitry A Pushin. Spin-orbit states of neutron wave packets. *Physical Review A*, 94(1):013605, 2016.

[91] SSR Oemrawsingh, X Ma, D Voigt, A Aiello, ER t Eliel, JP Woerdman, et al. Experimental demonstration of fractional orbital angular momentum entanglement of two photons. *Physical review letters*, 95(24):240501, 2005.

[92] Miles Padgett and Richard Bowman. Tweezers with a twist. *Nature photonics*, 5(6):343, 2011.

[93] Jian-Wei Pan, Dik Bouwmeester, Harald Weinfurter, and Anton Zeilinger. Experimental entanglement swapping: entangling photons that never interacted. *Physical Review Letters*, 80(18):3891, 1998.

[94] Jian-Wei Pan, Christoph Simon, Časlav Brukner, and Anton Zeilinger. Entanglement purification for quantum communication. *Nature*, 410(6832):1067, 2001.

[95] Arun K Pati. Minimum classical bit for remote preparation and measurement of a qubit. *Physical Review A*, 63(1):014302, 2000.

[96] Cheng-Zhi Peng, Jun Zhang, Dong Yang, Wei-Bo Gao, Huai-Xin Ma, Hao Yin, He-Ping Zeng, Tao Yang, Xiang-Bin Wang, and Jian-Wei Pan. Experimental long-distance decoy-state quantum key distribution based on polarization encoding. *Physical review letters*, 98(1):010505, 2007.

[97] Nicholas A Peters, Julio T Barreiro, Michael E Goggin, Tzu-Chieh Wei, and Paul G Kwiat. Remote state preparation: arbitrary remote control of photon polarization. *Physical review letters*, 94(15):150502, 2005.

[98] F Pfeiffer, C Grünzweig, O Bunk, G Frei, E Lehmann, and C David. Neutron phase imaging and tomography. *Physical Review Letters*, 96(21):215505, 2006.

[99] Franz Pfeiffer, Martin Bech, Oliver Bunk, Philipp Kraft, Eric F Eikenberry, Ch Brönnimann, Christian Grünzweig, and Christian David. Hard-x-ray dark-field imaging using a grating interferometer. *Nature materials*, 7(2):134, 2008.

[100] David Press, Thaddeus D Ladd, Bingyang Zhang, and Yoshihisa Yamamoto. Complete quantum control of a single quantum dot spin using ultrafast optical pulses. *Nature*, 456(7219):218, 2008.

[101] Robert Prevedel, Philip Walther, Felix Tiefenbacher, Pascal Böhi, Rainer Kaltenbaek, Thomas Jennewein, and Anton Zeilinger. High-speed linear optics quantum computing using active feed-forward. *Nature*, 445(7123):65, 2007.

[102] Brandon Redding, Sebastien M Popoff, and Hui Cao. All-fiber spectrometer based on speckle pattern reconstruction. *Optics express*, 21(5):6584–6600, 2013.

[103] Oscar G Rodríguez-Herrera, David Lara, Konstantin Y Bliokh, Elena A Ostrovskaya, and Chris Dainty. Optical nanoprobing via spin-orbit interaction of light. *Physical review letters*, 104(25):253601, 2010.

[104] Edward TF Rogers, Jari Lindberg, Tapashree Roy, Salvatore Savo, John E Chad, Mark R Dennis, and Nikolay I Zheludev. A super-oscillatory lens optical microscope for subwavelength imaging. *Nature materials*, 11(5):432, 2012.

[105] Joseph Samuel and Rajendra Bhandari. General setting for berry's phase. *Physical Review Letters*, 60(23):2339, 1988.

[106] Linda Sansoni, Fabio Sciarrino, Giuseppe Vallone, Paolo Mataloni, Andrea Crespi, Roberta Ramponi, and Roberto Osellame. Two-particle bosonic-fermionic quantum walk via integrated photonics. *Physical review letters*, 108(1):010502, 2012.

[107] D Sarenac, DG Cory, J Nsofini, I Hincks, P Miguel, M Arif, Charles W Clark, MG Huber, and DA Pushin. Generation of a lattice of spin-orbit beams via coherent averaging. *Physical review letters*, 121(18):183602, 2018.

[108] K Sawada and SP Walborn. Experimental quantum information processing with the talbot effect. *Journal of Optics*, 20(7):075201, 2018.

[109] Tobias Schaetz. Trapping ions and atoms optically. *Journal of Physics B: Atomic, Molecular and Optical Physics*, 50(10):102001, 2017.

[110] Erwin Schrödinger. Discussion of probability relations between separated systems. In *Mathematical Proceedings of the Cambridge Philosophical Society*, volume 31, pages 555–563. Cambridge University Press, 1935.

[111] Benjamin Schumacher. Sending entanglement through noisy quantum channels. *Physical Review A*, 54(4):2614, 1996.

[112] Yu-Bo Sheng and Fu-Guo Deng. One-step deterministic polarization-entanglement purification using spatial entanglement. *Physical Review A*, 82(4):044305, 2010.

[113] Peter W Shor. Polynomial-time algorithms for prime factorization and discrete logarithms on a quantum computer. *SIAM review*, 41(2):303–332, 1999.

[114] Harun H Solak, Christian Dais, and Francis Clube. Displacement talbot lithography: a new method for high-resolution patterning of large areas. *Optics express*, 19(11):10686–10691, 2011.

[115] Xin-Bing Song, Hai-Bo Wang, Jun Xiong, Kaige Wang, Xiangdong Zhang, Kai-Hong Luo, and Ling-An Wu. Experimental observation of quantum talbot effects. *Physical review letters*, 107(3):033902, 2011.

[116] Henry Fox Talbot. Lxxvi. facts relating to optical science. no. iv. *The London, Edinburgh, and Dublin Philosophical Magazine and Journal of Science*, 9(56):401–407, 1836.

[117] Wolfgang Tittel, Jürgen Brendel, Hugo Zbinden, and Nicolas Gisin. Quantum cryptography using entangled photons in energy-time bell states. *Physical Review Letters*, 84(20):4737, 2000.

[118] Juan P Torres, Yana Deyanova, Lluis Torner, and Gabriel Molina-Terriza. Preparation of engineered two-photon entangled states for multidimensional quantum information. *Physical Review A*, 67(5):052313, 2003.

[119] Rupert Ursin, F Tiefenbacher, T Schmitt-Manderbach, H Weier, Thomas Scheidl, M Lindenthal, B Blauensteiner, T Jennewein, J Perdigues, P Trojek, et al. Entanglement-based quantum communication over 144 km. *Nature physics*, 3(7):481, 2007.

[120] Giuseppe Vallone, Vincenzo DAmbrosio, Anna Sponselli, Sergei Slussarenko, Lorenzo Marrucci, Fabio Sciarrino, and Paolo Villoresi. Free-space quantum key distribution by rotation-invariant twisted photons. *Physical review letters*, 113(6):060503, 2014.

[121] P Van Loock, TD Ladd, K Sanaka, F Yamaguchi, Kae Nemoto, WJ Munro, and Y Yamamoto. Hybrid quantum repeater using bright coherent light. *Physical review letters*, 96(24):240501, 2006.

[122] Alipasha Vaziri, Jian-Wei Pan, Thomas Jennewein, Gregor Weihs, and Anton Zeilinger. Concentration of higher dimensional entanglement: qutrits of photon orbital angular momentum. *Physical review letters*, 91(22):227902, 2003.

[123] Lydia Vermeyden. Fundamental tests of quantum mechanics using two-photon entanglement. Master's thesis, University of Waterloo, 2014.

[124] Lydia Vermeyden, Xian Ma, Jonathan Lavoie, Madeleine Bonsma, Urbasi Sinha, Raymond Laflamme, and KJ Resch. Experimental test of environment-assisted invariance. *Physical Review A*, 91(1):012120, 2015.

[125] Philip Walther, Kevin J Resch, Terry Rudolph, Emmanuel Schenck, Harald Weinfurter, Vlatko Vedral, Markus Aspelmeyer, and Anton Zeilinger. Experimental one-way quantum computing. *Nature*, 434(7030):169, 2005.

[126] Albert Wang, Patrick Gill, and Alyosha Molnar. Light field image sensors based on the talbot effect. *Applied optics*, 48(31):5897–5905, 2009.

[127] Peng Wang and Rajesh Menon. Computational spectrometer based on a broadband diffractive optic. *Optics express*, 22(12):14575–14587, 2014.

[128] Xi-Lin Wang, Xin-Dong Cai, Zu-En Su, Ming-Cheng Chen, Dian Wu, Li Li, Nai-Le Liu, Chao-Yang Lu, and Jian-Wei Pan. Quantum teleportation of multiple degrees of freedom of a single photon. *Nature*, 518(7540):516, 2015.

[129] Jianming Wen, Yong Zhang, and Min Xiao. The talbot effect: recent advances in classical optics, nonlinear optics, and quantum optics. *Advances in optics and photonics*, 5(1):83–130, 2013.

[130] G Wendin. Quantum information processing with superconducting circuits: a review. *Reports on Progress in Physics*, 80(10):106001, 2017.

[131] JH Wesenberg, A Ardavan, GAD Briggs, JJL Morton, RJ Schoelkopf, DI Schuster, and Klaus Mølmer. Quantum computing with an electron spin ensemble. *Physical review letters*, 103(7):070502, 2009.

[132] Alan E Willner, Hao Huang, Yan Yan, Yongxiong Ren, Nisar Ahmed, Goudong Xie, Changjing Bao, L Li, Y Cao, Z Zhao, et al. Optical communications using orbital angular momentum beams. *Advances in Optics and Photonics*, 7(1):66–106, 2015.

[133] FNC Wong, JH Shapiro, and T Kim. Efficient generation of polarization-entangled photons in a nonlinear crystal. *Laser physics*, 16(11):1517–1524, 2006.

[134] FangZhou Wu, GuoJian Yang, HaiBo Wang, Jun Xiong, Faris Alzahrani, Aatef Hobiny, and FuGuo Deng. High-capacity quantum secure direct communication with two-photon six-qubit hyperentangled states. *Science China Physics, Mechanics & Astronomy*, 60(12):120313, 2017.

[135] Saijun Wu, Edward Su, and Mara Prentiss. Demonstration of an area-enclosing guided-atom interferometer for rotation sensing. *Physical review letters*, 99(17):173201, 2007.

[136] Xing-Can Yao, Tian-Xiong Wang, Ping Xu, He Lu, Ge-Sheng Pan, Xiao-Hui Bao, Cheng-Zhi Peng, Chao-Yang Lu, Yu-Ao Chen, and Jian-Wei Pan. Observation of eight-photon entanglement. *Nature photonics*, 6(4):225, 2012.

[137] Nanfang Yu and Federico Capasso. Flat optics with designer metasurfaces. *Nature materials*, 13(2):139, 2014.

[138] Zhen-Sheng Yuan, Yu-Ao Chen, Bo Zhao, Shuai Chen, Jörg Schmiedmayer, and Jian-Wei Pan. Experimental demonstration of a bdcz quantum repeater node. *Nature*, 454(7208):1098, 2008.

[139] Yifan Zhao and Jian Wang. High-base vector beam encoding/decoding for visible-light communications. *Optics letters*, 40(21):4843–4846, 2015.

[140] Zhi Zhao, Tao Yang, Yu-Ao Chen, An-Ning Zhang, and Jian-Wei Pan. Experimental realization of entanglement concentration and a quantum repeater. *Physical review letters*, 90(20):207901, 2003.

APPENDICES

Appendix A

Python code for OAM lattice simulation

A.1 Define the field generated by LOV prism pairs

Note: This code is written by Sacha Schwarz in 2018.

```
def Ux(x,x0,rc):
    sigmaX=np.matrix([[0,1],[1,0]])
    return (np.cos(np.pi*(x-x0)/(2*rc))*np.identity(2)
            +1j*np.sin(np.pi*(x-x0)/(2*rc))*sigmaX)

def Uy(y,y0,rc):
    sigmaY=np.matrix([[0,-1j],[1j,0]])
    return (np.cos(np.pi*(y-y0)/(2*rc))*np.identity(2)
           +1j*np.sin(np.pi*(y-y0)/(2*rc))*sigmaY)
```

Here is the function defined for LOV-field with an explanation for all variables used.

```
def LOV_field(N,X,Y,x0,y0,rc
              ,phi_IN,ket_meas
              ,w0):
```

```
            for k in range(dim):
                 for kk in range(dim):
                     x=X[k,kk]
                     y=Y[k,kk]
                     field[kk,k] = np.dot(np.conjugate(ket_meas).T
                        ,(Ux(x,x0,rc)*Uy(y,y0,rc))**N*phi_IN)

           field=np.exp(-(X**2+Y**2)/w0**2)*field
           return field

'''Explanation for LOV_field function:
   Generates transversal distribution of LOV prisms (with interferometry and
   plotting option) for given input and projection state

   INPUT
   -----
   N:              int
                   sets of LOV prism pairs
   X:              ndarray
                   2D x axis meshgrid array
   Y:              ndarray
                   2D y axis meshgrid array
   x0:             float
                   zero position of x
   y0:             float
                   zero position of y
   rc:             float
                   smallest radial distance at which the polarization
                   undergoes a pi-rotation
   phi_IN:         ndarray
                   polarization state as input
   ket_meas:       ndarray
                   polarization state as input
   w0:             float
                   beam waist of transversal Gaussian intensity distribution
```

```
    OUTPUT
    ------
    field:  ndarray
            LOV_field(X,Y) values for input meshgrid X,Y with parameters
            N,x0,y0,rc,phi_IN,ket_meas,w0,kx,ky,phi_x and phi_y
    '''
```

A.2 Plotting simulation results of the intensity distribution

Now, I plug in parameters of our LOV prism pairs and set the beam waist (w0) to be what we generated in the lab ($25/3\ mm$). The polarization of the incoming beam is set to be $|L\rangle$ and we post-select on $|R\rangle$ after $N = 2$ sets of LOV prism pairs.

```
nSamples=2**10 #we have 1024*1024 pixels

theta=2*np.pi/180 #prism angle
lambda0=0.808 #wavelength of our beam
dn=0.0091 # birefringence of LOV prism (circular quartz wedges)
a=lambda0/(dn*np.tan(theta))

x0=0
y0=0
rc=a/2

limits=25/3*(10**3)  #We use micrometers in the code
vec=np.linspace(-limits,limits,nSamples)
X,Y=np.meshgrid(vec,vec)

field = [LOV_field(2,X,Y,x0,y0,rc,phi_IN=ket_L(),ket_meas=ket_R()
        ,w0=25/3*(10**3),grayPlots=False)]
```

The simulation outputs the intensity distribution seen in Fig. A.1. In the lab our images are not as bright so only the middle 3×3 lattice is visible. We crop the simulated images by setting the limitation of $x-$ axis and $y-$ axis to the same region.

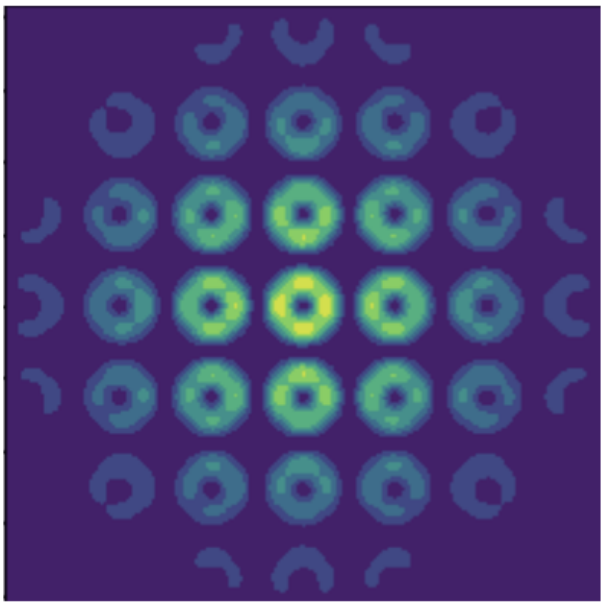

Figure A.1: Simulated OAM lattice with all parameters used in the lab

Here I give an example of the Python code for generating Fig. 3.1. First, we generate the intensity distribution with parameters used in the lab:

```
phi_IN_vec=[ket_H(),ket_V(),ket_D(),ket_A(),ket_L(),ket_R()]

nSamples=2**10
theta=2*np.pi/180
lambda0=0.808
dn=0.0091 # birefringence of LOV prism (circular quartz wedges)
a=lambda0/(dn*np.tan(theta))

x0=0
y0=0
rc=a/2
N=2
w0=25/3*(10**3)

limits=25/3*(10**3)
```

```
vec=np.linspace(-limits,limits,nSamples)
X,Y=np.meshgrid(vec,vec)

theoField=np.zeros((len(phi_IN_vec),nSamples,nSamples),dtype='complex')
for k in range(len(phi_IN_vec)):
    theoField[k,:,:]=LOV_field(N,X,Y,x0,y0,rc,phi_IN=phi_IN_vec[k]
                    ,ket_meas=ket_R(),w0=w0,plots=True)
```

Then, we crop the simulated images to match the visible region observed in the lab and plot them nicely.

```
sidePos= a
lim=4e3
xPlotLimits=[-lim,lim]
yPlotLimits=[-lim,lim]
fontSize=18

fig,ax=plt.subplots(3,2,figsize=(10,10))

for j in range(3):
    for i in range(2):
        p=ax[j,i].contourf(X,Y,np.abs(theoField[2*j+i,:,:])**2,100, cmap='inferno')
        ax[j,i].set_aspect('equal')
        plt.sca(ax[j,i])
        plt.xlim(xPlotLimits)
        plt.xticks([-sidePos,0,sidePos], ['-a', '0', 'a'], fontsize=fontSize)
        plt.ylim(xPlotLimits)
        plt.yticks([-sidePos,0,sidePos], ['-a', '0', 'a'], fontsize=fontSize)

    cbar=fig.colorbar(p, ax=ax[j].ravel().tolist())
    cbar.solids.set_edgecolor("face")
    cbar.set_label('Intensity', fontsize=fontSize, labelpad=10)
    cbar.set_ticks(np.arange(0, 1.1,0.25))
plt.show()
```